J Therm Spray Tech (2017) 26:1356–1380
DOI 10.1007/s11666-017-0580-3

PEER REVIEWED

Effect of Particle Morphology on Cold Spray Deposition of Chromium Carbide-Nickel Chromium Cermet Powders

Ruben Fernandez[1] · **Bertrand Jodoin**[1]

Submitted: 14 February 2017 / in revised form: 25 May 2017 / Published online: 12 June 2017

Abstract Nickel chromium-chromium carbide coatings provide good corrosion and wear resistance at high temperatures, making them ideal for applications where a harsh environment and high temperatures are expected. Thermal spray processes are preferred as deposition technique of cermets, but the high process temperatures can lead to decarburization and reduction of the coatings properties. Cold spray uses lower temperatures preventing decarburization. Since the metallic phase remains solid, the feedstock powder morphology becomes crucial on the deposition behavior. Six commercially available powders were studied, varying in morphology and metal/ceramic ratios. The powders were categorized into 4 groups depending on their morphology. Spherical powders lead to substrate erosion due to their limited overall ductility. Porous agglomerated and sintered powders lead to severely cracked coatings. For dense agglomerated and sintered powders, the outcome depended on the initial metal/ceramic ratio: powders with 25 wt.% NiCr led to substrate erosion while 35 wt.% NiCr powders led to dense coatings. Finally, blended ceramic-metal mixtures also lead to dense coatings. All coatings obtained had lower ceramic content than the initial feedstock powders. Interrupted spray tests, combined with FEA, helped drawing conclusions on the deposition behavior to explain the obtained results.

Keywords cermet · chromium carbide · cold spray · deposition behavior · finite element analysis · NiCr

---

✉ Ruben Fernandez
rufernan@ing.uchile.cl

[1] University of Ottawa Cold Spray Research Laboratory, Ottawa, ON, Canada

Introduction

Chromium carbide-based cermets are materials generally employed for wear, abrasion and erosion protection due to their high hardness (Ref 1-4). Nickel alloys are often used for the matrix material to provide good corrosion/oxidation protection in high-temperature environments (Ref 3, 5). Investigations have shown that they can operate in harsh environments at temperatures up to 900 °C (Ref 6-10). These properties make cermets ideal for operating conditions where erosion is expected as well as corrosive environments, such as combustion chambers and high-temperature turbines (Ref 11, 12). These materials also find applications at ambient temperature where corrosion and erosion resistance are required (Ref 7).

Chromium carbide-nickel chromium cermets (CrC-NiCr) are normally applied as coatings on top of a base material. Thermal spray processes are the preferred manufacturing methods to produce these coatings, with HVOF and plasma spraying being the most commonly used. The high temperature involved in these processes allows melting the NiCr phase and obtaining low-porosity coating with a high deposition efficiency. The main drawback of these high-temperature spraying processes is related to the sensitivity of chromium carbides to high temperatures. The elevated gas process temperatures (3000 °C for HVOF and 10000 °C for plasma spraying) can lead to decarburization which results in reduced coating properties (Ref 6). This drawback of thermal spray processes is present for other cermet coatings as well such as WC-Co (Ref 13-15). Cold spray has been explored as an alternative process to overcome this drawback (Ref 14, 16).

The cold spray process accelerates feedstock powders (usually metals) in a supersonic gas stream produced by a convergent-divergent nozzle (De Laval) (Ref 17-19). Due

Table 1 Summary of powders used

Commercial name	Production method	Composition, wt.% carbide/metal	Particle size range, µm	Feed rate, g/min	In-flight velocity, m/s
Praxair CRC-410	Atomized	70/30	−45/+11	32.7 ± 3.7	435 ± 92
Praxair CRC-425	Atomized	60/40	−45/+11	31.8 ± 4.3	430 ± 85
Praxair CRC-300	Agglomerated and sintered	75/25	−45/+11	13.5 ± 2.2	451 ± 98
H.C. Starck Amperit 584	Agglomerated and sintered	75/25	−45/+10	21.1 ± 1.2	499 ± 143
H.C. Starck Amperit 587	Agglomerated and sintered	65/35	−45/+10	17.0 ± 2.7	509 ± 151
Oerlikon Diamalloy 3004	Atomized with crushed	75/25	−45/+5	21.3 ± 3.3	471 ± 175

Table 2 Cold spray parameters used

Parameter	Value
Gas temperature	500 °C
Gas pressure	3.8 MPa
Gas nature	Nitrogen
Traverse speed	5 mm/s
Passes	5
Feed conditions	240 holes wheel at 5 RPM
Standoff distance	10 mm

Table 3 Material properties used in FEA simulations

	Ni20Cr (Ref 49)	Steel AISI 4340 (Ref 37)	Cr_3C_2 (Ref 50-52)
k, W/m K	11.3	16	12
ρ, kg/m^3	8400	7830	6600
G, GPa	87	79.6	…
E, GPa	…	…	373
v	…	…	0.21
C_p, J/kg K	450	477	551.66

Table 4 Johnson-Cook parameters used in simulations

Johnson-Cook parameter	Inconel 718 (Ref 53)	Steel AISI 4340 (Ref 37)
A, MPa	450	792
B, MPa	1700	510
C	0.017	0.033
n	0.65	0.26
m	1.3	1.03
$\dot{\varepsilon}_{ref}$	0.001	1
T_m, K	1570	1793
T_{ref}, K	298	293

Table 5 Mie-Gruneisen parameters used in simulations

Parameters	Monel (Ref 54)	Steel AISI 4340 (Ref 54)
Gruneisen constant, Γ_0	1.95	1.67
Speed of sound, m/s	4190	4578
Hugoniot slope, s	1.54	1.33

to the low gas temperatures used in addition to the rapid gas expansion in the nozzle, the feedstock powders remain solid throughout their flight making cold spray a solid-state process (Ref 20-22). The particles impact the substrate and experience extensive plastic deformation, bonding the particles to the substrate either mechanically or if enough plastic deformation is obtained metallurgically (Ref 20-25). Cermet coatings have been produced by cold spray by blending ceramic particles into the feedstock metallic powders (Ref 26-29). For these cases, the ceramic particles do not experience plastic deformation upon impact and only a fraction of the ceramic particles present in the feedstock powder are retained in the coating (Ref 29, 30). Powders prepared with different techniques have been sprayed, such as agglomerated and sintered WC-Co powders (Ref 31-33). In these cases, higher velocities are needed to obtain a coating, as the particles are difficult to deform (Ref 31-33). The production of a successful coating using these powders typically requires higher operating temperatures and pressures and often helium as main gas, making the process less appealing for industrial applications. Due to the operating temperatures in cold spray, decarburization can be avoided. As such, when a coating is obtained, it normally possesses higher wear resistance and denser microstructures than coatings produced by other thermal spray processes (Ref 31-33).

The deposition of the initial layer of CrC-NiCr powders by cold spray has not been extensively studied, although important studies have been performed to address the potential of several CrC-NiCr powders in producing wear and corrosion resistance coatings (Ref 34, 35). Since cold spray is a solid-state process, the powder morphology becomes a key factor in the deposition behavior of these particles, in particular of the first layer on the substrate. In this investigation, six different commercially available CrC-NiCr powders were studied. These powders presented different morphologies and ceramic/metal ratios. The powders deposition behavior was investigated by assessing deposition efficiency, observing single-particles impacts and FEA modeling of the particle impacts. The goal of this study is to assess with a descriptive approach the effect of the cermet morphology on the cold spray deposition behavior of the initial layer of chromium carbide-nickel chromium powders and subsequent coating buildup and support the studies previously done with these materials (Ref 34).

Experimental Procedures

Materials and Production Methods

Six different commercially available CrC-NiCr feedstock powders were studied. The powders were produced by four different production methods. CRC-410 and CRC-425 powders (Praxair Surface Technologies, Indianapolis, IN, USA) were used. They are atomized powders with 30 wt.% and 40 wt.% NiCr, respectively. Three agglomerated and sintered powders were also used: CRC-300 (Praxair Surface Technologies, Indianapolis, IN, USA), Amperit 584 and Amperit 587 (H.C. Starck, Munich, Germany). CRC-300 and Amperit 584 have a composition of 25 wt.% NiCr, and Amperit 587 has a composition of 35 wt.% NiCr. Finally, the commercially available blended powder Diamalloy 3004 (Oerlikon Metco Inc., Westbury, NY, USA) was also used. This powder is made of crushed chromium

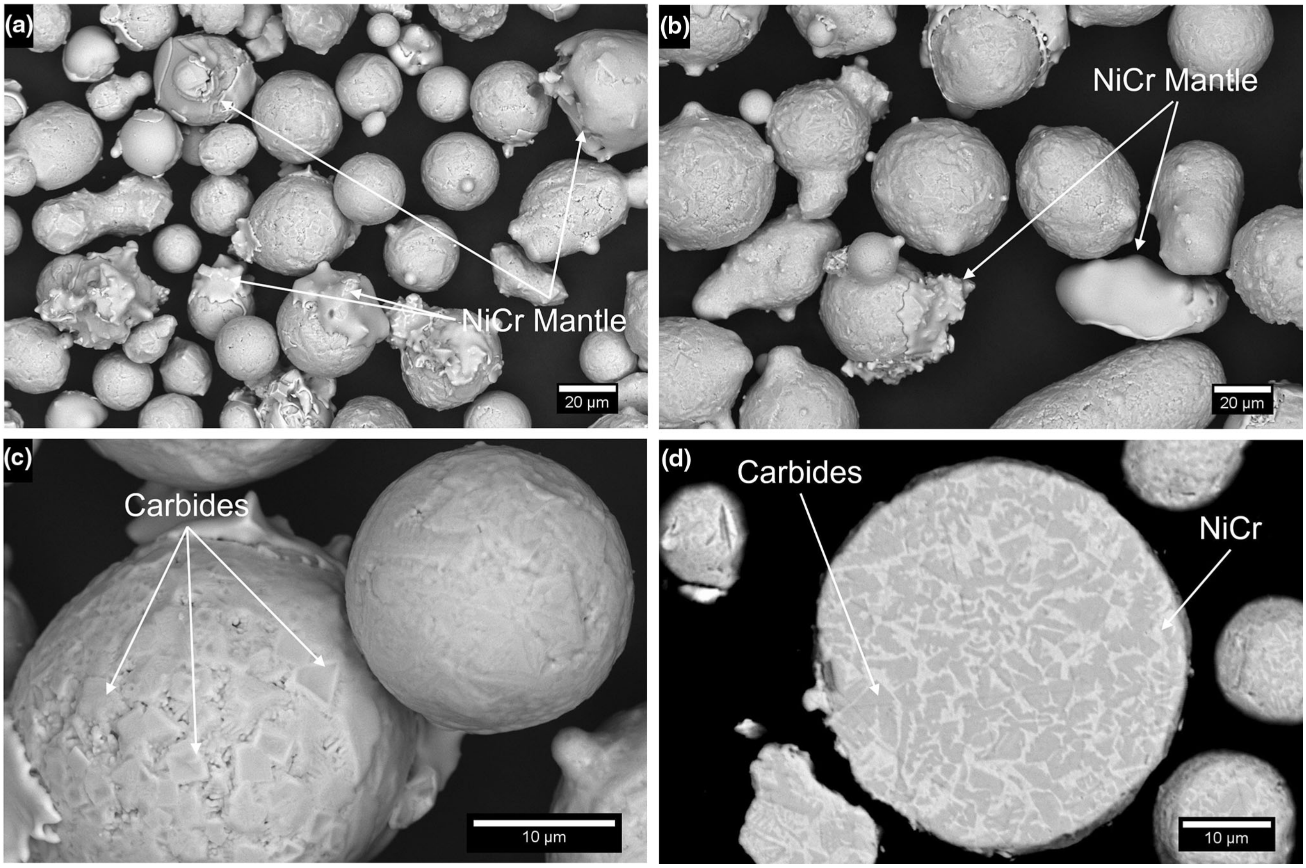

Fig. 1 Overview of powders: (a) CRC-410; (b) CRC-425; (c) details of CRC-425; (d) cross section of a CRC-410 particle

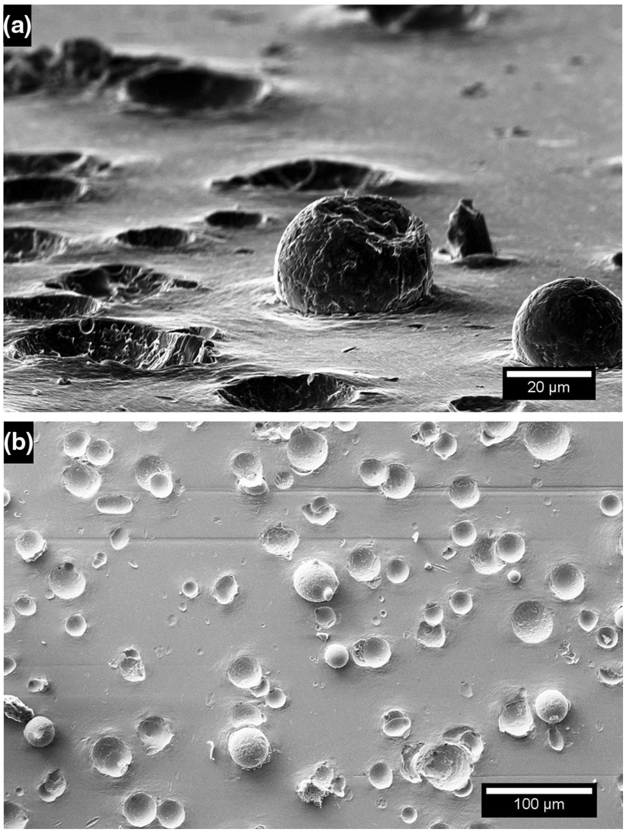

Fig. 2 Overview of interrupted spray test for: (a) CRC-410 powder; (b) CRC-415 powder

carbide and atomized NiCr with a composition of 25 wt.% NiCr. Table 1 summarizes the feedstock powders used, detailing the production method, composition and powder size range. The selected material for the substrate was AISI 4340 steel with a hardness of 340 HV.

Cold Spray Deposition

The cold spray system used was the commercially available EP Series SST High Pressure Cold Spray System (Centerline Ltd., Windsor, Ontario, Canada). The system consists of a 15-kW heater with a maximum gas temperature of 500 °C and a maximum gas pressure of 3.8 MPa. The De Laval nozzle used for this work has a throat diameter of 2 mm and a diverging section length and exit diameter of 120 and 6.35 mm, respectively. The powder was fed using a commercially available powder feeder (Model AT-1200HP, Thermach Inc., Appleton, WI, USA). All sprays were performed using the spray parameters given in Table 2. It is important to mention that the maximum gas temperature and pressure that can be reached by the system were used in the experiments.

The deposition efficiency (DE) of each feedstock powder was calculated. The powder feed rate and the substrate weight were measured prior and post-deposition. A precision scale Sartorius Extend—model ED124S, with a readability of 1 mg was used for weighing the substrate. Table 1 presents the feed rates measured per powder used.

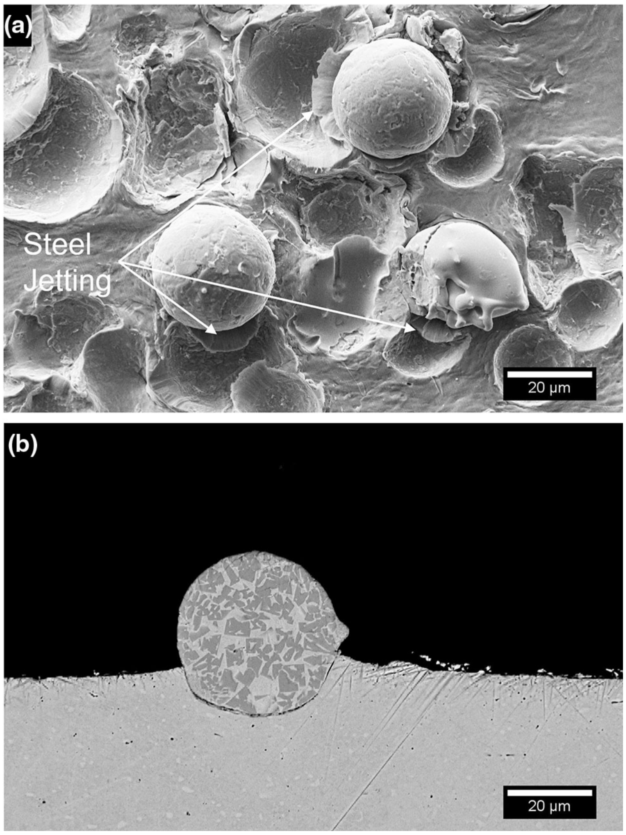

Fig. 3 (a) Details of interrupted spray test of CRC-410 powders, showing jetting of the steel substrate; (b) cross section of a CRC-415 deposited particle

Interrupted spray tests were performed to evaluate individual particle deposition. They consist in interrupting the powder feeding while continuing the raster pattern with the spray nozzle. It produces traces on the substrate with zones where no particle have hit, zones where single impacts have occurred, zones where the first complete layer of coating has been produced and zones where a full coating is formed. These tests help to give insights into the powders deposition behavior.

Powders and Coatings Characterization

The as-received feedstock powder morphology was analyzed through secondary and backscattered electron modes using a scanning electron microscope (SEM, model EVO MA-10, Carl Zeiss AG, Oberkochen, Germany). Powders were also cross-sectioned and analyzed in order to observe the ceramic and metal distributions inside the feedstock particles. The powders composition was evaluated using

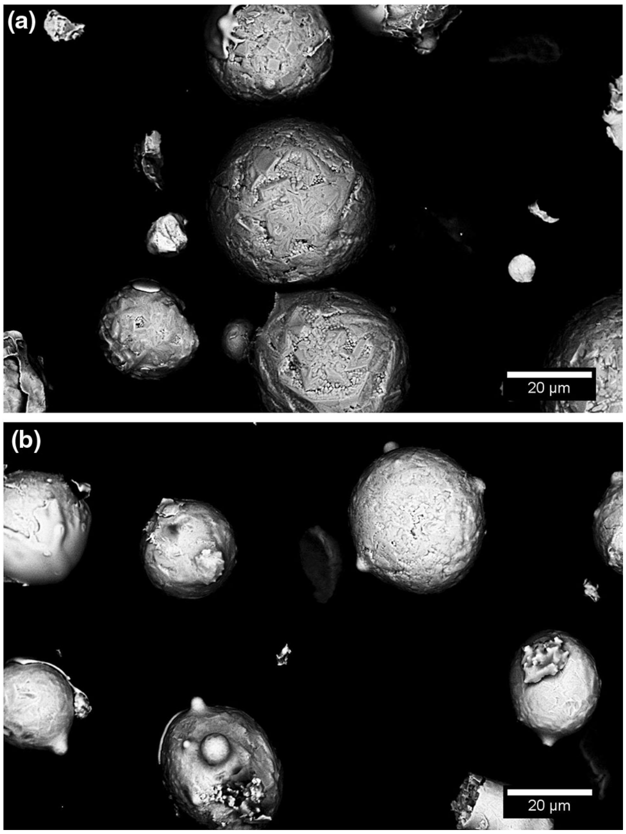

Fig. 4 Recovered powder after deposition: (a) CRC-410; (b) CRC-425

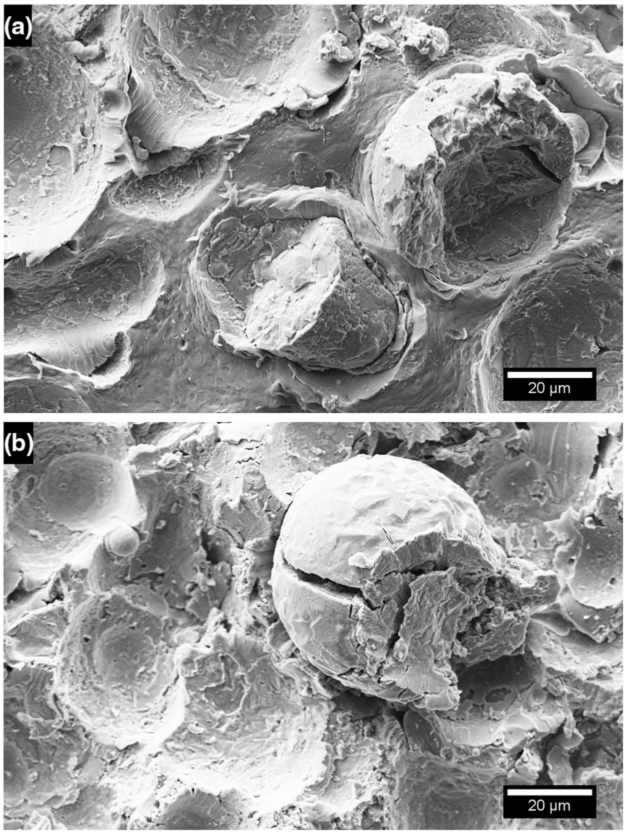

Fig. 5 Adhered particles fractured by incoming particles: (a) CRC-410; (b) CRC-425

energy-dispersive x-ray spectroscopy (EDS, model INCA X-Act, Oxford Instruments, Oxford, England).

To get a better insight of the deposition process, as-sprayed not adhered particles were also analyzed by SEM. These particles were recovered by locating an adhesive carbon tape in the vicinity of the substrate during deposition and were analyzed under SEM. The coatings and interrupted spray test samples produced were cross-sectioned and examined using an optical microscope (VHX-1000, Keyence Corporation, Osaka, Japan) and a SEM. The powder and coating compositions were evaluated using EDS.

Finite Element Analysis

A plane strain 2D finite element analysis was performed in order to evaluate and understand the powder deformation dynamics upon impact. Since different powder morphologies may potentially lead to different deformation mechanisms, powder particle cross sections were digitalized in order to obtain the proper morphology required for the simulations. The digitalization of the images was based on the contrast of the cross-sectioned images. BSD images were used to obtain different contrasts for the different material phases. This allowed to differentiate the metal and the ceramic phases in the particle. A software was developed in the open-source Simple Morphological Image Library (SMIL) software to process these images and extract the morphology of the particles and the ceramic content. The data points were then exported using a Python-Abaqus script into a sketch to proceed with the simulation. Any particular inconsistency in the sketch creation process was fixed manually. The material properties used were determined by the nature of the phase identified. It is important to mention that irregular particles are rarely modeled in cold spray simulation as it is a labor-intensive process (Ref 36) and FEA analysis of cermet particles has not been found in the literature. It is expected that the impact modeling proposed in this work will help to explain the different impact and buildup behaviors of the different powders examined. The software Abaqus/Explicit was employed to carry out these analyses. A quad-dominated mesh was used based on 4-node coupled temperature-displacement elements (CPE4RT). Although a 2D simulation presents the limitation of not perfectly representing the particles, the modeling strategy used allows to incorporate the material inhomogeneity in a simple morphological representation. This allows studying the

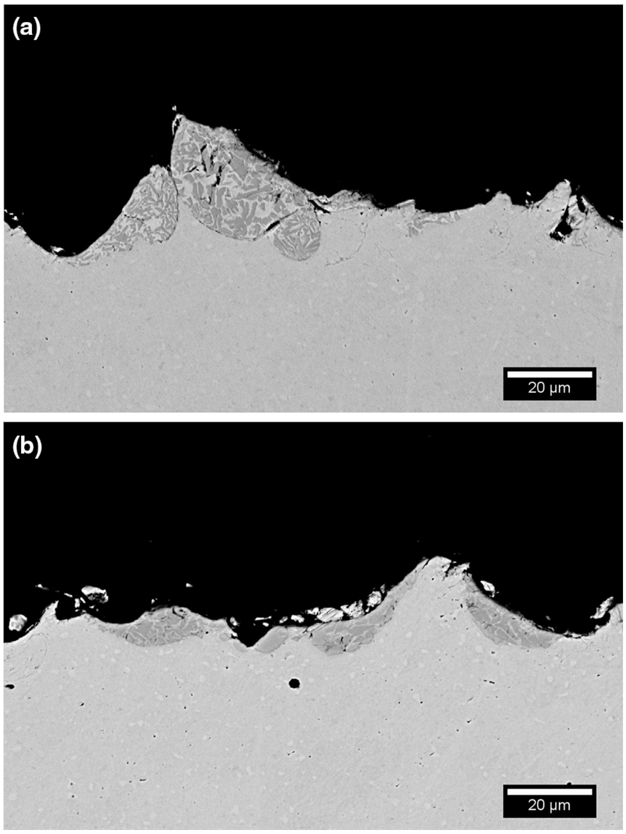

Fig. 6 Cross section of interrupted spray tests in zones with multiple impacts: (a) two layers tentatively sprayed; (b) several layers tentatively sprayed

interaction between the metallic and ceramic phases during the particle impacts. The modeling results obtained were compared with the interrupted spray tests in order to validate the results.

For the simulations, the Johnson-Cook constitutive equation (Eq 1) was used to model the plastic behavior of the metallic phases (Ref 37). The state equation used was the linear Us-Up Hugoniot form of Mie-Gruneisen (Eq 2). These equations have been used in several investigations to describe particles and substrates deformations in cold spray (Ref 38-43). It is important to mention that no damage criteria were included in the analysis.

$$\sigma_{\mathrm{eq}} = \left[A + B\varepsilon_{\mathrm{p}}^{n}\right]\left[1 + C\ln\left(\frac{\dot{\varepsilon}_{\mathrm{p}}}{\dot{\varepsilon}_{\mathrm{ref}}}\right)\right]\left[1 - \left(\frac{T - T_{\mathrm{ref}}}{T_{\mathrm{m}} - T_{\mathrm{ref}}}\right)^{m}\right] \quad \text{(Eq 1)}$$

$$p = \frac{\rho_0 c_0^2 \eta}{(1 - s\eta)^2}\left(1 - \frac{\Gamma_0 \eta}{2}\right) - \Gamma_0 \rho_0 E_m, \quad \eta = 1 - \frac{\rho_0}{\rho} \quad \text{(Eq 2)}$$

A, B, C, n, m, $\dot{\varepsilon}_{\mathrm{ref}}$ and T_{ref} are the Johnson-Cook parameters, ε_{p} is the plastic strain, $\dot{\varepsilon}_{\mathrm{p}}$ is the plastic strain rate, T is the temperature of the material and T_{m} is the melting point.

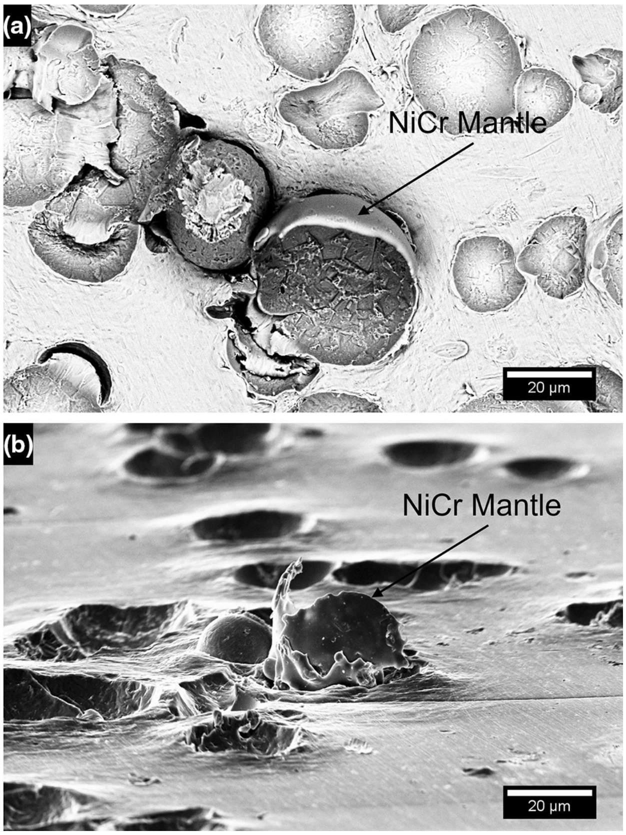

Fig. 7 Details of remaining NiCr shells seen after the interrupted spray tests

In Eq 2, p is the hydrodynamic stress, ρ_0 is the initial density, ρ is the actual density, c_0 is the material speed of sound, s is the Hugoniot slope, Γ_0 is the Gruneisen constant and E_m is the energy per unit mass.

NiCr material properties were used for the metallic phase, while steel AISI 4340 was used for the substrate and the elastic properties of Cr_3C_2 were employed for the ceramic phase. A summary of those properties is presented in Table 3. It is important to mention that for the plastic behavior of the metallic phase, the NiCr properties were approximated as those of nickel alloy (Inconel 718), due to the unavailability of required NiCr properties in the literature. This alloy was chosen since its chemical composition resembles the one of the NiCr metallic phase. Although this change in the properties can slightly alter simulation results, the overall effect of the cermet morphology on the deformation behavior is expected to remain valid. A similar obstacle was encountered for the equation of state. In that case, the parameters of Monel were used for the metallic phase. The parameters used can be found in Tables 4 and 5. It is important to mention that the carbide used in the FEA and present in the powders is Cr_3C_2 for all powders except CRC-410 and CRC-425. In these two powders, a generic chromium carbide is declared by the

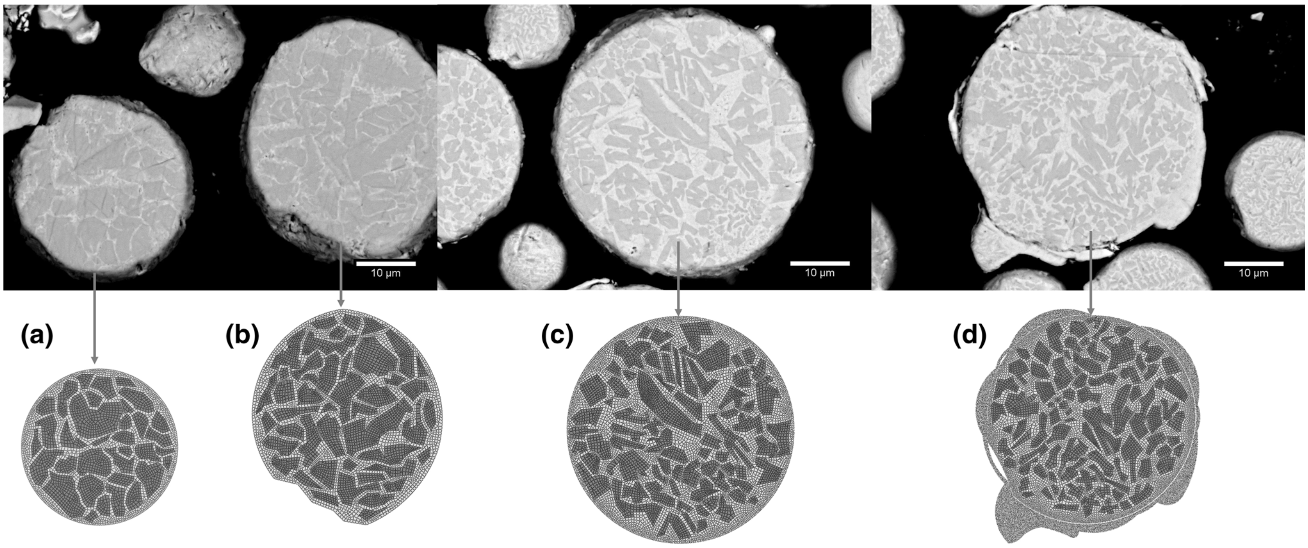

Fig. 8 Digitalization of particles used in the simulations. Particles (a) and (b) are from powder CRC-410 and (c) and (d) from powder CRC-425

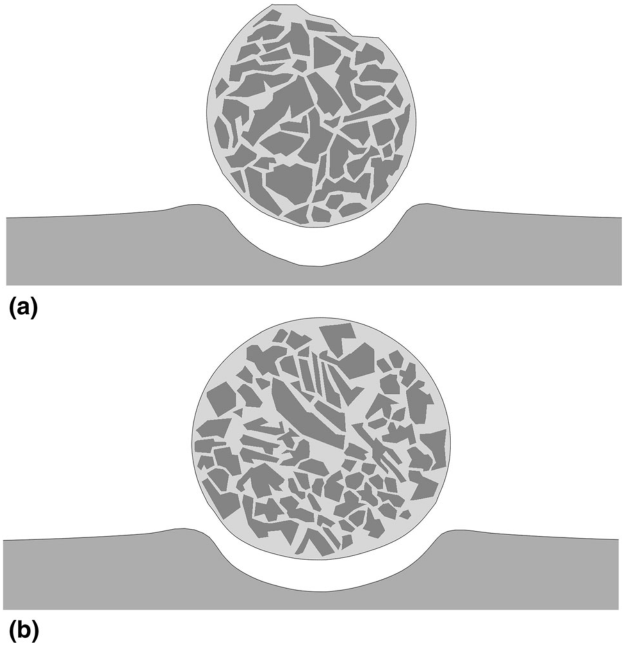

Fig. 9 FEA results of impacts of: (a) CRC-410 particle; (b) CRC-425 particle, 1 μs after rebound

manufacturer. The presence of other carbides (Cr_7C_3 or $Cr_{23}C_6$) can have an influence on the deposition behavior of the particles.

The particle velocities required for the model inputs were measured using a Cold Spray Meter (CSM) eVOLUTION (Tecnar Automation Ltd, St-Bruno, Canada). This system performs in-flight diagnostic by illuminating the particles with a continuous 2.4-W ($\lambda = 810$ nm) laser and capturing the reflection through a dual split photomask in order to calculate the particles velocity. The obtained velocities per powder can be found in Table 1. The substrate temperature used in the model was measured using a FLIR i7 portable infrared camera. Finally, the particle impact temperature was assumed to be 80% of the gas stagnation temperature, similar to values calculated in previous investigations (Ref 44). For particles and substrates, a quadratic mesh was used with a coupled temperature-displacement element type (CPE4RT). The maximum element size of 0.5 μm was used. Arbitrary Lagrangian-Eulerian (ALE) adaptive domain was used for the substrates and metallic phase mesh. The results were directly compared to the interrupted spray test results to evaluate the deposition behavior of the particles.

Results and Discussion

Powder morphology was observed for the six different feedstock powders studied. Four distinctive morphology categories were defined based on what was observed: CRC-410 and CRC-425 were categorized as spherical, CRC-300 as porous agglomerated and sintered, Amperit 584 and Amperit 587 as dense agglomerated and sintered, and finally Diamalloy 3004 as blended. In the following section, the description of the results of deposition behavior, interrupted spray tests and the FEA are separated according to the powder categories.

Spherical Morphology

Both CRC-410 and CRC-425 atomized powders were categorized as spherical. These powders are morphologically similar, presenting a spherical structure characteristic of atomized powders. The powders show several ceramic particles inside a metallic matrix. Figure 1(a) and

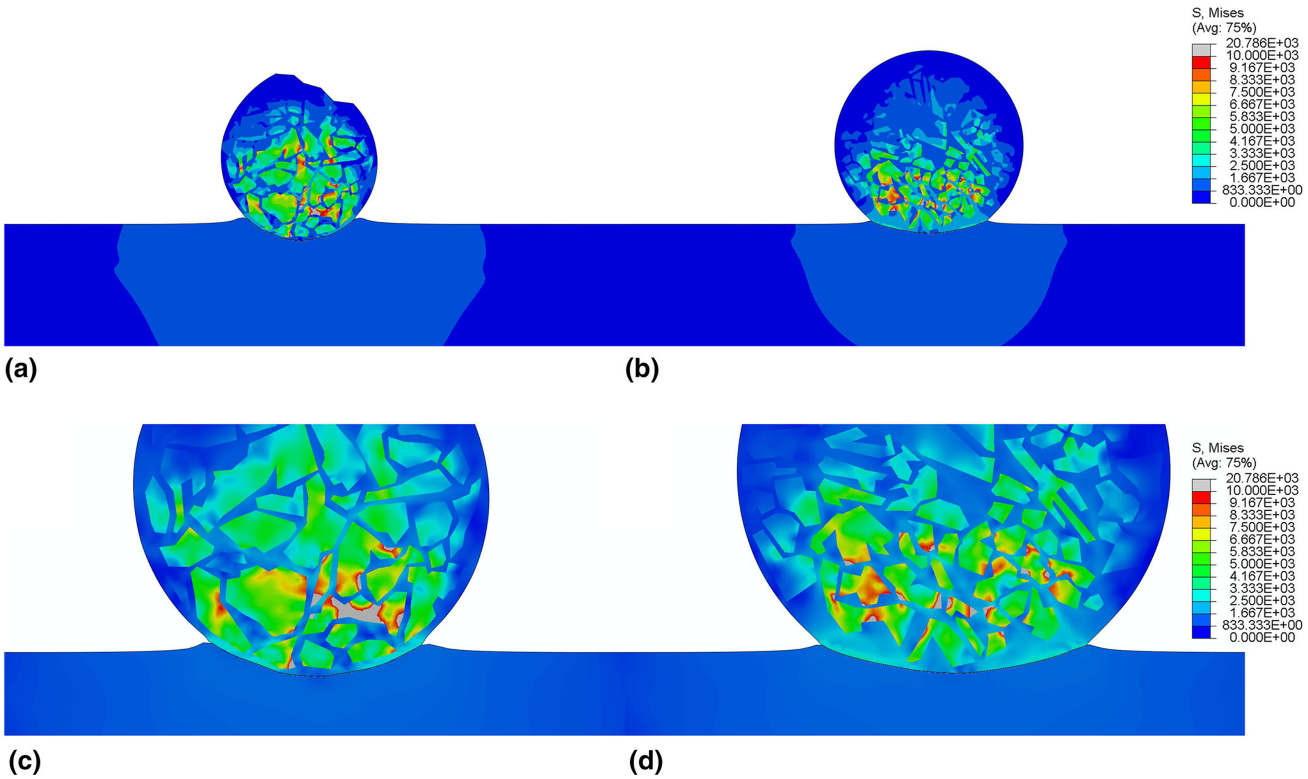

Fig. 10 Overall and details of stress distributions upon impact of particles: (a) and (c) CRC-410 particle; (b) and (d) CRC-425 particle

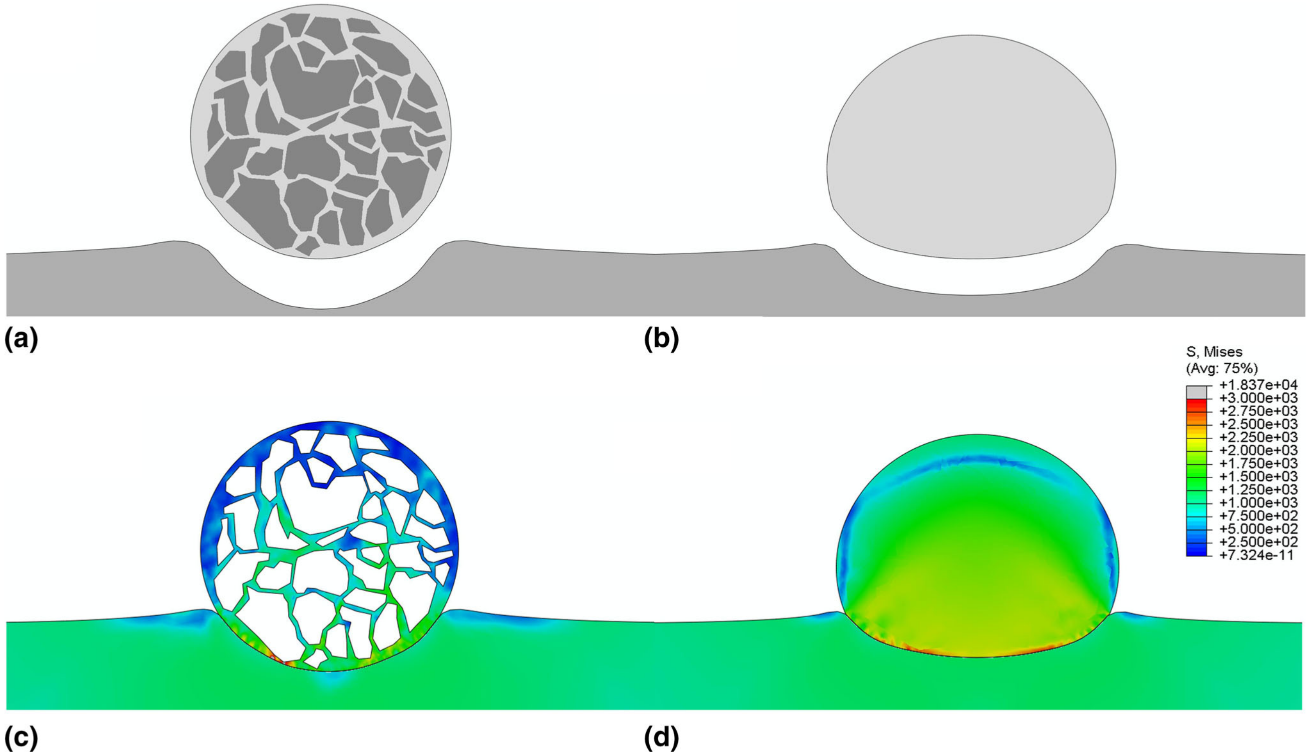

Fig. 11 Comparison of particles: (a) with ceramic; (b) only metallic; (c) stress distribution of particle with ceramics; (d) stress distribution of only metallic particle

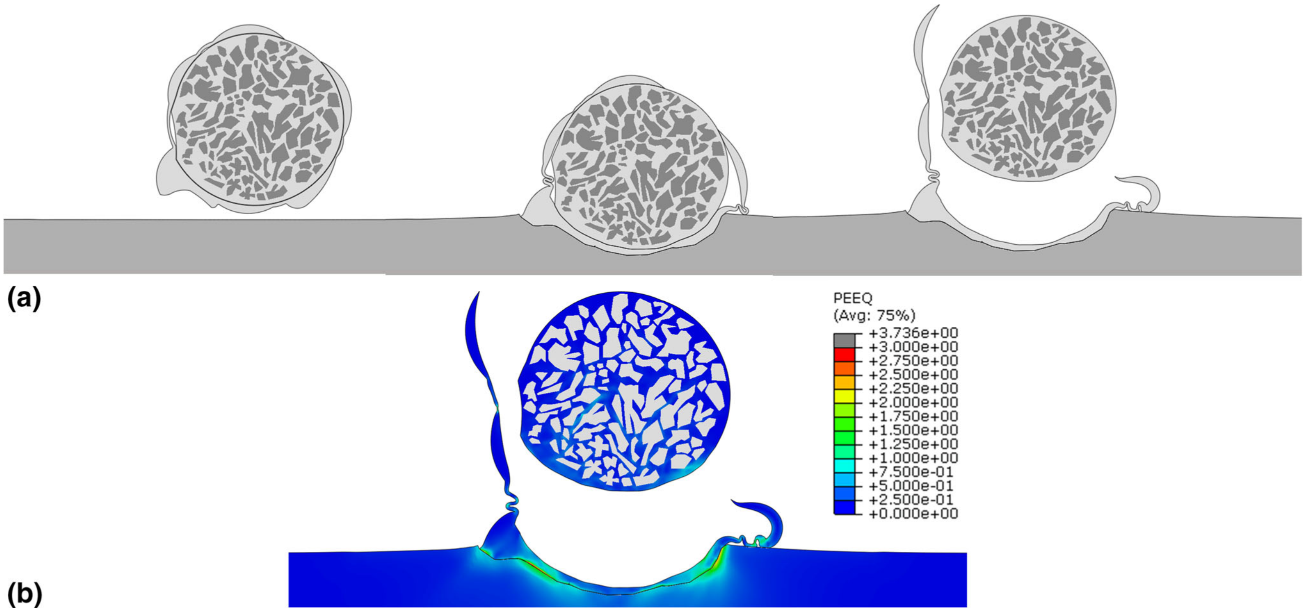

Fig. 12 FEA results of particle showing NiCr mantle: (a) deformation behavior/stages; (b) equivalent plastic deformation

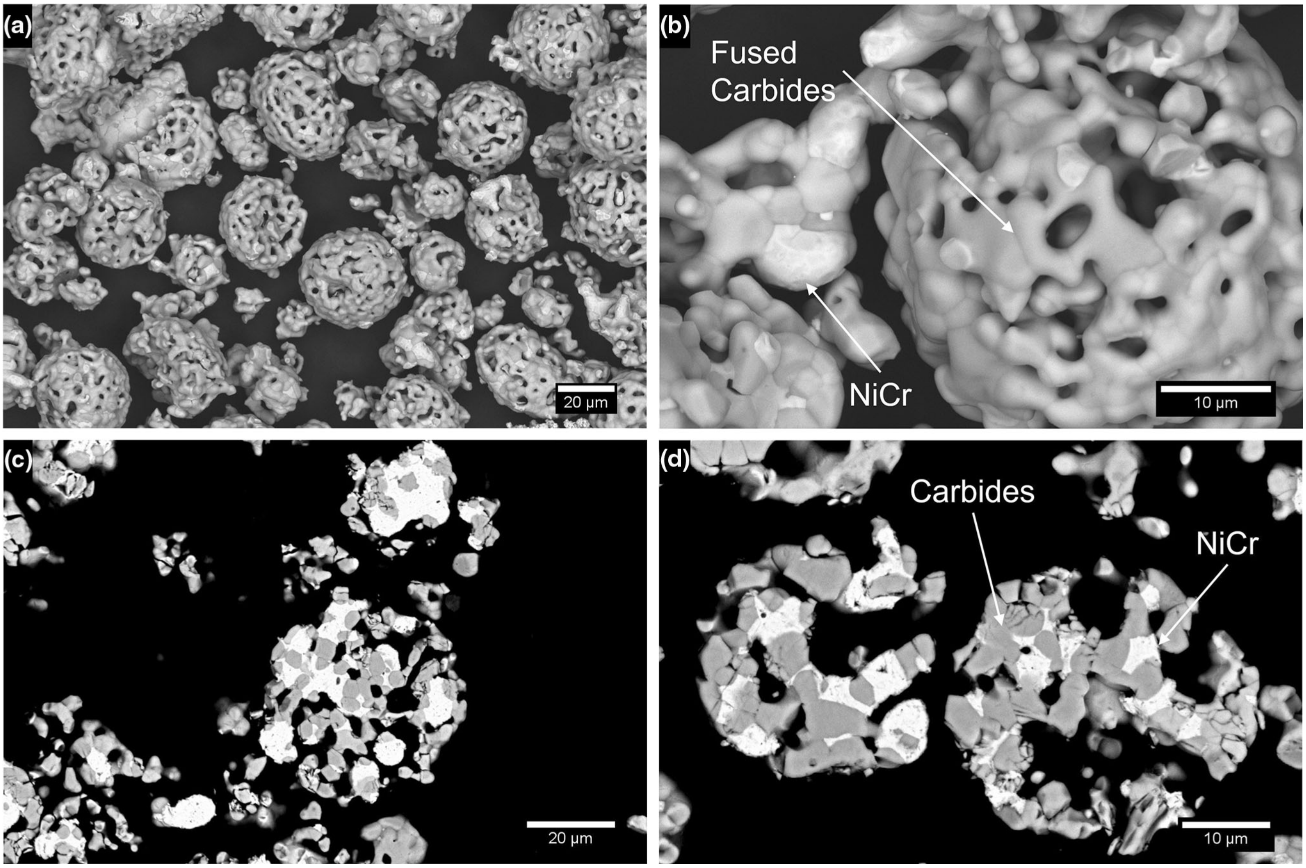

Fig. 13 (a) Overview of CRC-300 powders; (b) superficial details of the particles; (c) and (d) cross sections of particles

(b) shows the CRC-410 and CRC-425 powders, respectively, establishing their morphological similarities. Figure 1(c) shows details at the surface of the CRC-425 powder where ceramic phases can be observed. Figure 1(d) shows a representative cross section of one CRC-410 particle, showing the carbide distribution, represented

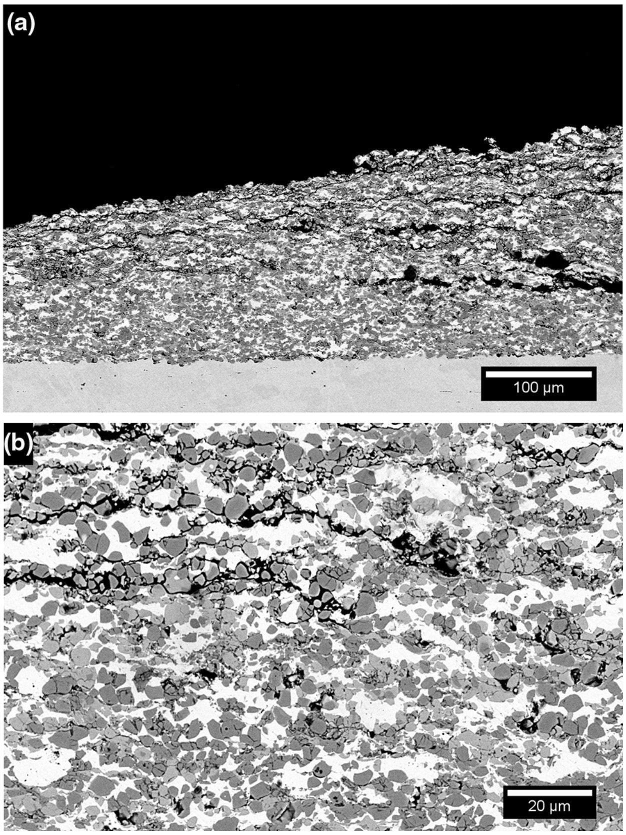

Fig. 14 Cross sections of CRC-300 coatings

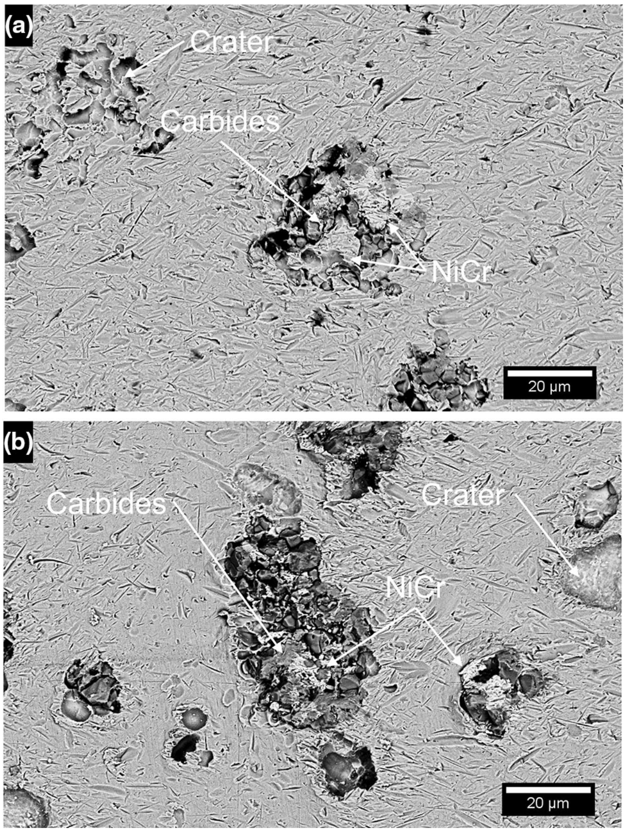

Fig. 15 Top view of single particle impact showing a fractured CRC-300 particle

as the darker particles in the BSD image, and the NiCr represented as the whiter matrix. It can be seen that the powder particles are dense and that the ceramic is uniformly distributed inside the particles. It can be noted that some of the particles appear to have a smooth coat at the surface, as can be observed in Fig. 1(b). This was identified as NiCr. It is possible that during the atomization, some of the droplets had no ceramic particles suspended in the liquid metallic phase and some of them impacted and solidified on other particles, coating them with a thin metallic layer.

Neither of these powders resulted in a successful coating. The spray process rather led to erosion of the steel substrate. This was corroborated by the DE measurement, yielding for CRC-410 and CRC-425 values of −0.6 and −0.4%, respectively. The interrupted spray tests gave some insights into the spray process of these powders with results that were similar for both spherical powders. Figure 2 shows an overview of the tests results. Clear indentations of the cermet particles are observed on the substrates, and a few adhered particles are observed at the substrates surface.

Examination of Fig. 3(a) reveals some details about the powders deposition behavior. Multiple deep spherical indentations in the steel substrates are visible with a clear imprint of the particles surface. The presence of severe material jetting can be found in the craters surroundings. EDS analysis identified that this jetting occurred solely in the substrate. Even though the high-strength steel substrates show these signs of severe deformation, the cermet particles show a complete lack of deformation, demonstrating the high hardness of these cermet powders. This lack of deformation is shown in cross-sectional images of the interrupted spray tests, such as Fig. 3(b). It reveals that the particles are still spherical even below the substrate surface. This result is also confirmed when analyzing the recovered powder particles after the spraying process. Figure 4(a) and (b) shows representative powder particles recovered, illustrating that the particles have not experienced deformation upon impact.

In zones of high impact rate, it is possible to see locations where the incoming particles interacted with the few adhered particles at the substrate surface. When these interactions occur, the adhered particles either get dislodged from the substrate leaving an indentation or get fractured. This lack of ductility also makes the incoming particle unable to adhere to a previously deposited particle. Consequently, the creation of a second layer of particles is limited, preventing coating buildup. Figure 5 shows a few particles that have been impacted by incoming particles:

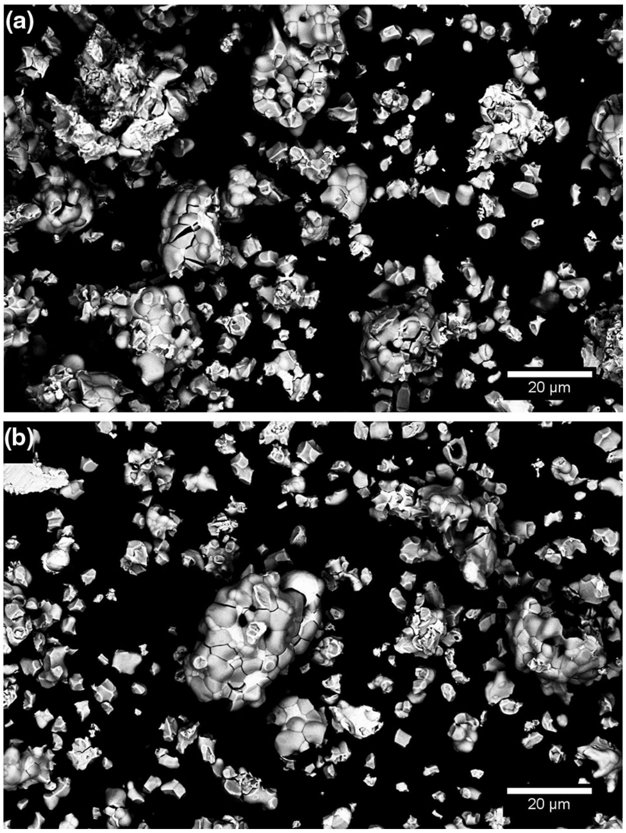

Fig. 16 Overview of non-adhered recovered CRC-300 powder (a) fractured particles; and (b) full particles cracked in ceramic sections

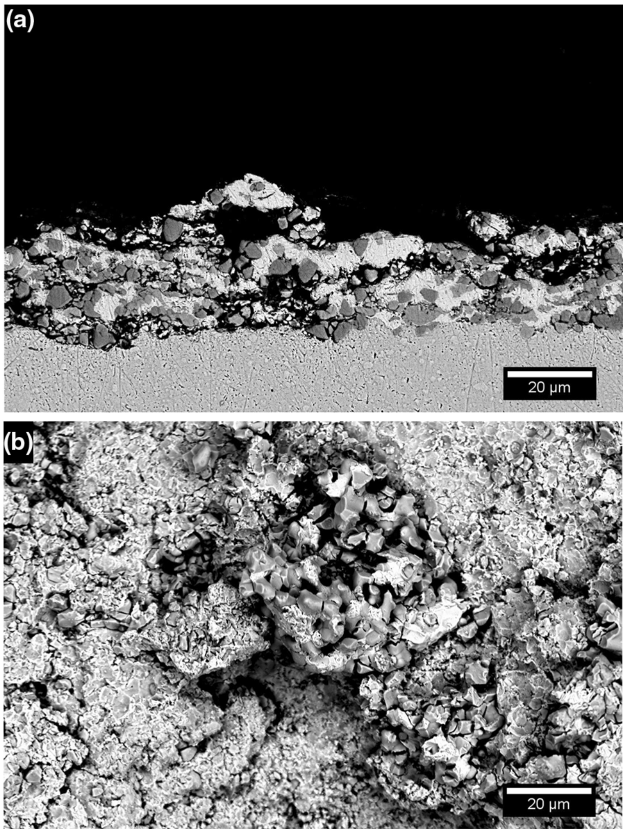

Fig. 17 (a) Cross section; (b) top view, of the second layer of adhering CRC-300 particles

the particles are fractured and show minor level of plastic deformation.

The overall spraying outcome of this kind of particles (with low ductility) is similar to the deposition of ceramics, where a particle gets embedded in the soft substrate and is almost instantly eroded by the incoming particles leaving small embedded sections on the substrate. This is confirmed by substrate cross sections where several layers were tentatively sprayed. Figure 6(a) shows particles that have been impacted by a second wave of incoming particles and shows eroded and fractured sections, while Fig. 6(b) shows the final substrate after several of these layers were tentatively sprayed, with only traces of particles remaining on a highly deformed surface.

Another phenomenon observed from the interrupted spray test images is related to the NiCr layer found at the surface of some of the particles mentioned previously. When these particles hit the substrate surface, it appears that this layer can achieve bonding with the substrate as several of these particles sections were found at the surface of the test samples. Some of these sections are presented in Fig. 7. This NiCr mantle was always found without the inner particle suggesting that this outer layer has no strong bonding with the particle itself. This observation is another indication that the particle does not adhere due to the lack of ductility. Since these layers are metallic, they have the ductility required to deform and adhere to the substrate while the hard particles do not show this ductility, bouncing back upon impact.

Finite element analysis helps to further explain the reasons behind the powders deposition behavior. The particles were cross-sectioned, and several representative particles were digitalized and exported to Abaqus/Explicit in order to perform impact simulation. Figure 8 shows some of the digitalized particles that were used in the simulation. The NiCr and Cr_3C_2 phases were also traced based on the images contrasts in order to represent the internal microstructure of the particles. It is worth mentioning that a particle coated with a NiCr layer (mantle) was digitalized, and it is represented by particle D in Fig. 8. The mantle was modeled as a separate element from the particle, and it was assumed that no attachment exists between these parts. From the figure, one can notice the difference in NiCr composition between particles A and B (CRC-410) versus particle C and D (CRC-425), as the latter ones contain a higher amount of the metallic phase. For the finite element analysis, a total of three particles per

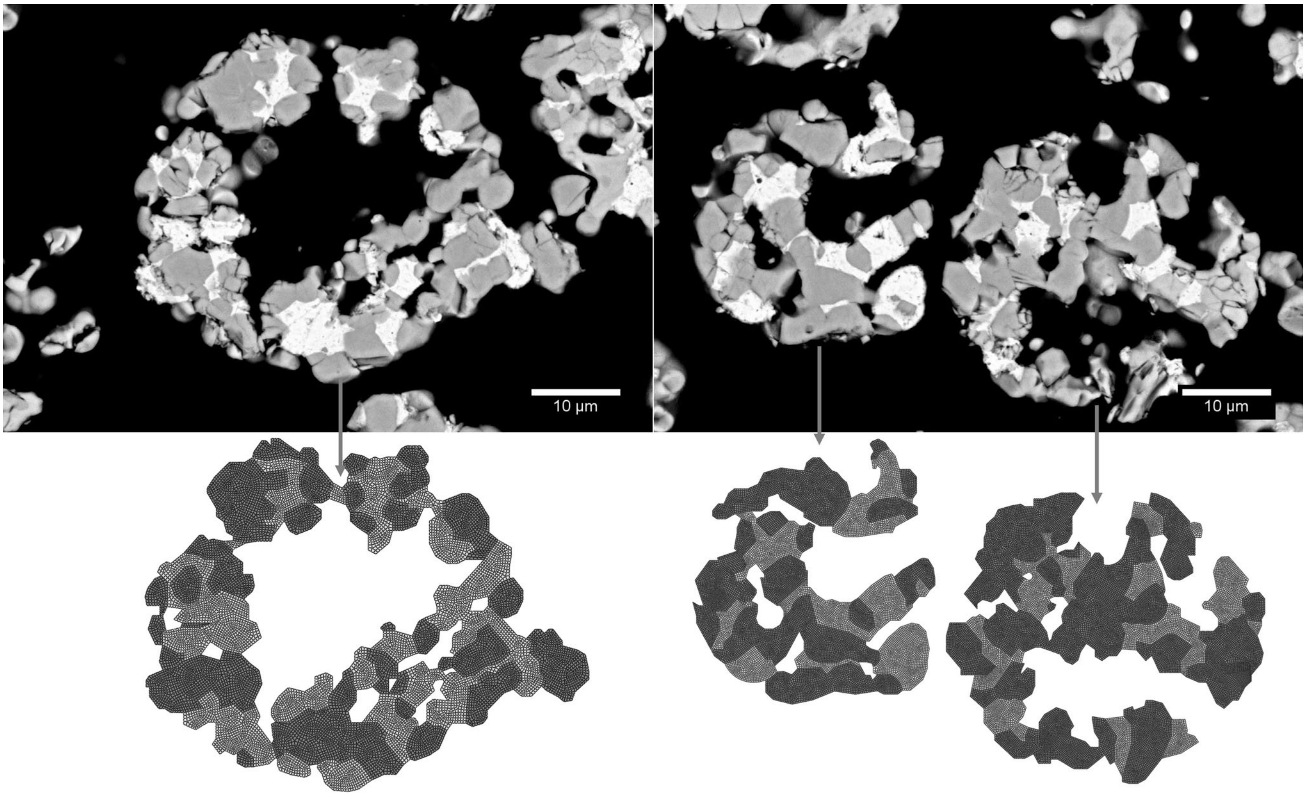

Fig. 18 Particle digitalization for CRC-300 powders

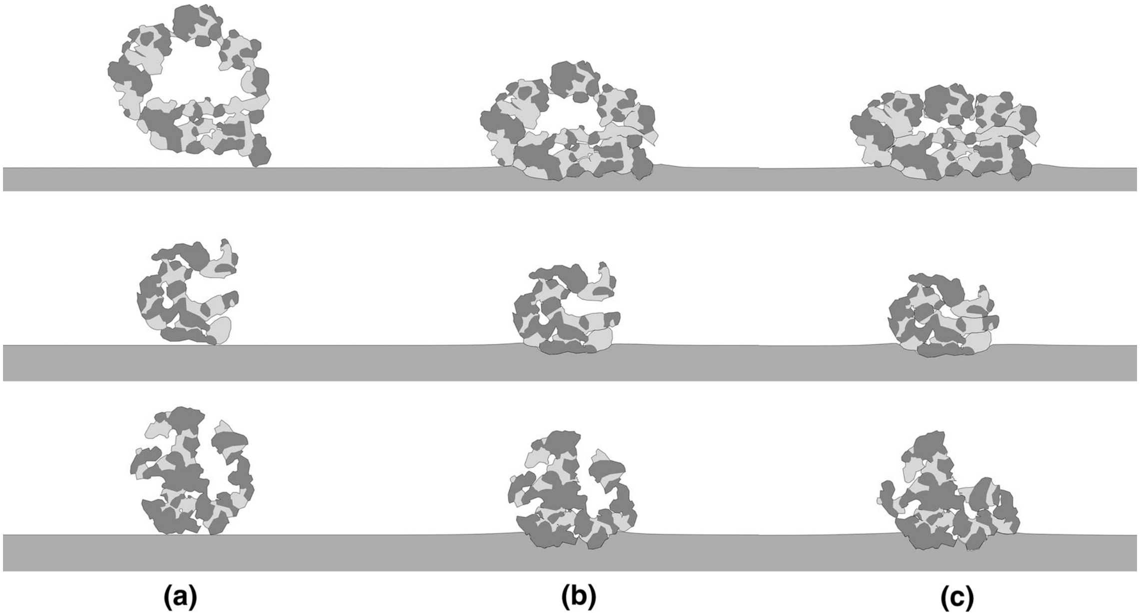

Fig. 19 Evolution of 3 CRC-300 particles deformation at different kinetic energy levels: (a) highest kinetic energy level; (b) midpoint; (c) lowest kinetic energy level

powder type were digitalized. The substrate temperature was evaluated at 192 °C using thermal imaging.

Similar to the results observed experimentally, the finite element analysis also shows a limited degree of particle deformation, as presented in Fig. 9. Even in the case of the CRC-425 powder particles, where higher metallic content is present, the analysis displays very little deformation of the particle. However, the substrate experienced a high

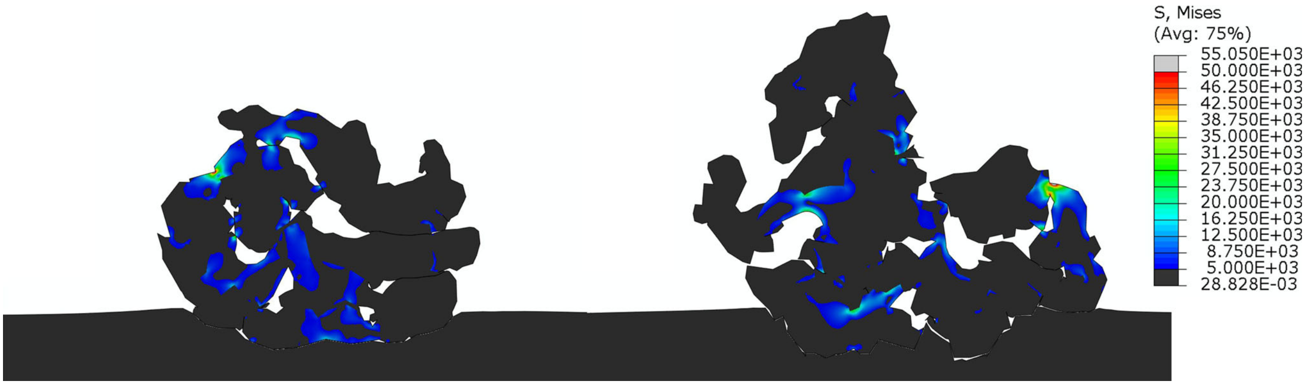

Fig. 20 FEA results: stress fields in two selected CRC-300 Particles

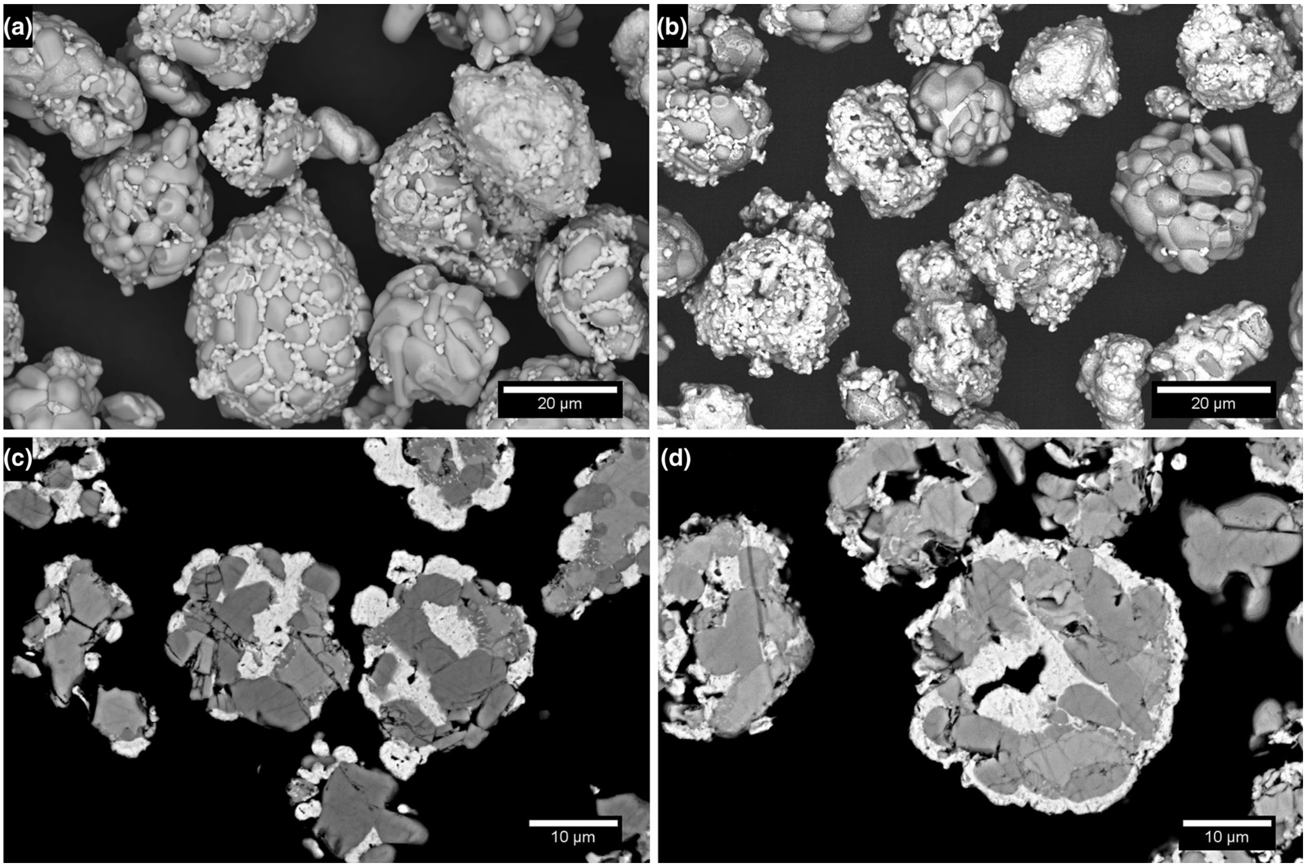

Fig. 21 Overview and cross sections of powders: (a) and (c) Amperit 584; (b) and (d) Amperit 587

degree of deformation showing the origins of the deep indentations seen in the experimental results.

This behavior is explained by the uniformly distributed ceramic phase inside the particles. Figure 10 shows the modeled stress distributions during the particle impacts. It is observed that the highest stresses are found in the particles ceramic phase. These ceramic zones redistribute the stresses uniformly across the particles enhancing their strength and inhibiting their ductility. As such, the lower stress levels experienced by the ductile phase are insufficient to induce shear instability that is usually responsible for particle deformation and bonding in cold spray.

This stress redistribution mechanism was corroborated by comparing the modeled deformation states of the

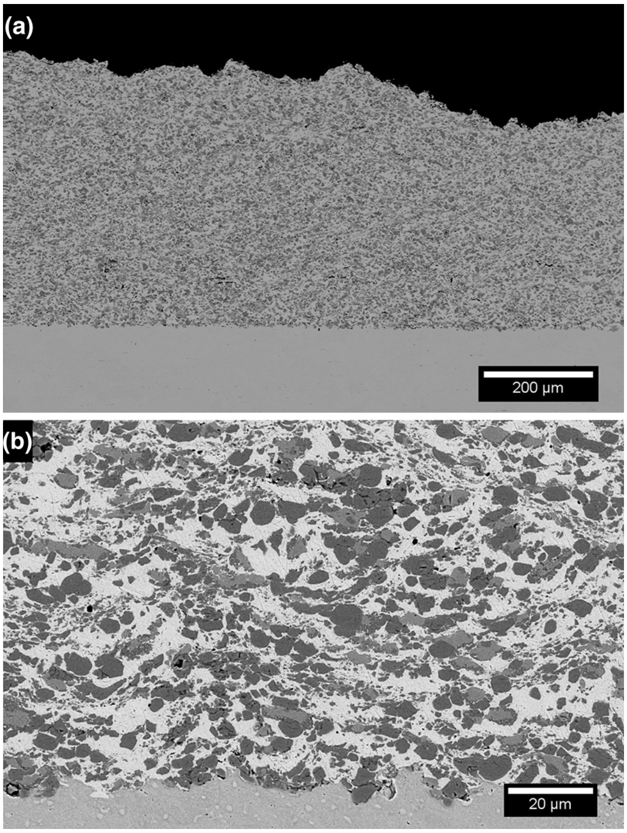

Fig. 22 Coatings cross sections obtained with Amperit 587: (a) overview; (b) details at the interface

particles used for this study with a simulation of a particle consisting of the metallic phase only. The results are presented in Fig. 11. This figure clearly shows the impact that the ceramic elements have on the deformation behavior of the particles and the stress redistribution due to the ceramic particles. Figure 11(c) and (d) shows the stress field in the particles during the impact, where the ceramic phase was removed from the image in order to directly compare the metallic phases stress.

This strengthening mechanism is the same as the one behind the enhanced strength and hardness of cermet materials and is the reason why cermets are good candidates for abrasion resistant materials. This mechanism is also the reason behind the lower DE exhibited by these particles compared to the ones made of solely the metallic phase and explains why they are less suitable to be sprayed by cold spray. Since cold spray is a solid-state process that relies on extensive plastic deformation to obtain adhesion, these cermet particles are too densely distributed in the matrix, and under the spray conditions used they were no able to reach the deformation level needed to adhere to the substrate and therefore cause erosion. It is possible that at higher particle impact velocity and temperature that can be reached with high-pressure cold spray equipment, these particles can meet the conditions to obtain the adiabatic shear instability needed for bonding. This should be explored in further investigation.

The impact modeling of the coated NiCr mantle showed a different behavior where a high degree of deformation of the mantle is observed. Figure 12(a) shows three stages of the particle undergoing impact. The first stage shows the particle an instant before the impact. During the second stage, the substrate and mantel are undergoing large plastic deformations, and the mantle starts delaminating from the particle core. Finally, the last stage, a few moments after the impact, shows that the inner particle has bounced off and that the mantle is still in contact with the substrate. This result closely resembles the one seen in Fig. 7. Figure 12(b) shows the computed equivalent plastic deformation (PEEQ) during the last stage. It is important to notice the high amount of plastic deformation experienced by the mantle while the particle core did not show any significant deformation. By undergoing a high amount of plastic deformation, the mantle has larger probabilities to adhere to the substrate, and this was simulated by not allowing separation between the mantle and the substrates in the FEA model. These modeling results support and help to explain the presence of similar structures found at the surface of interrupted spray tests substrates.

Porous Agglomerated and Sintered Morphology

Based on its morphology, the CRC-300 powder was identified as porous agglomerated and sintered. Figure 13(a) and (b) shows an overview of the powder size and morphology as well as details of the surface of this powder. One can observe that the powder particles are porous and the ceramic particles appear to have fused during the sintering process. In these powders, the NiCr component act as a binder for the ceramic particle, gluing sections of fused ceramic particles rather than a metallic matrix containing the ceramic phase as found in the previous powders (CRC-410 and CRC-425). The powder internal microstructure is presented in Fig. 13(c) and (d) were cross sections of the powders are shown and its porosity is better revealed.

The deposition efficiency of this powder was evaluated at 1.7%. Despite this low value, a coating was successfully sprayed. It is important to note that during deposition sections of the built coating flaked off, due to low adhesion. The DE was calculated without considering these flaked sections. Cross sections of these coatings are shown in Fig. 14, revealing several horizontal cracks. This might be a result of the feedstock powder porosity combined with a lack of plasticity or deformation of the particles upon impact. It is hypothesized that these cracks and the flaking

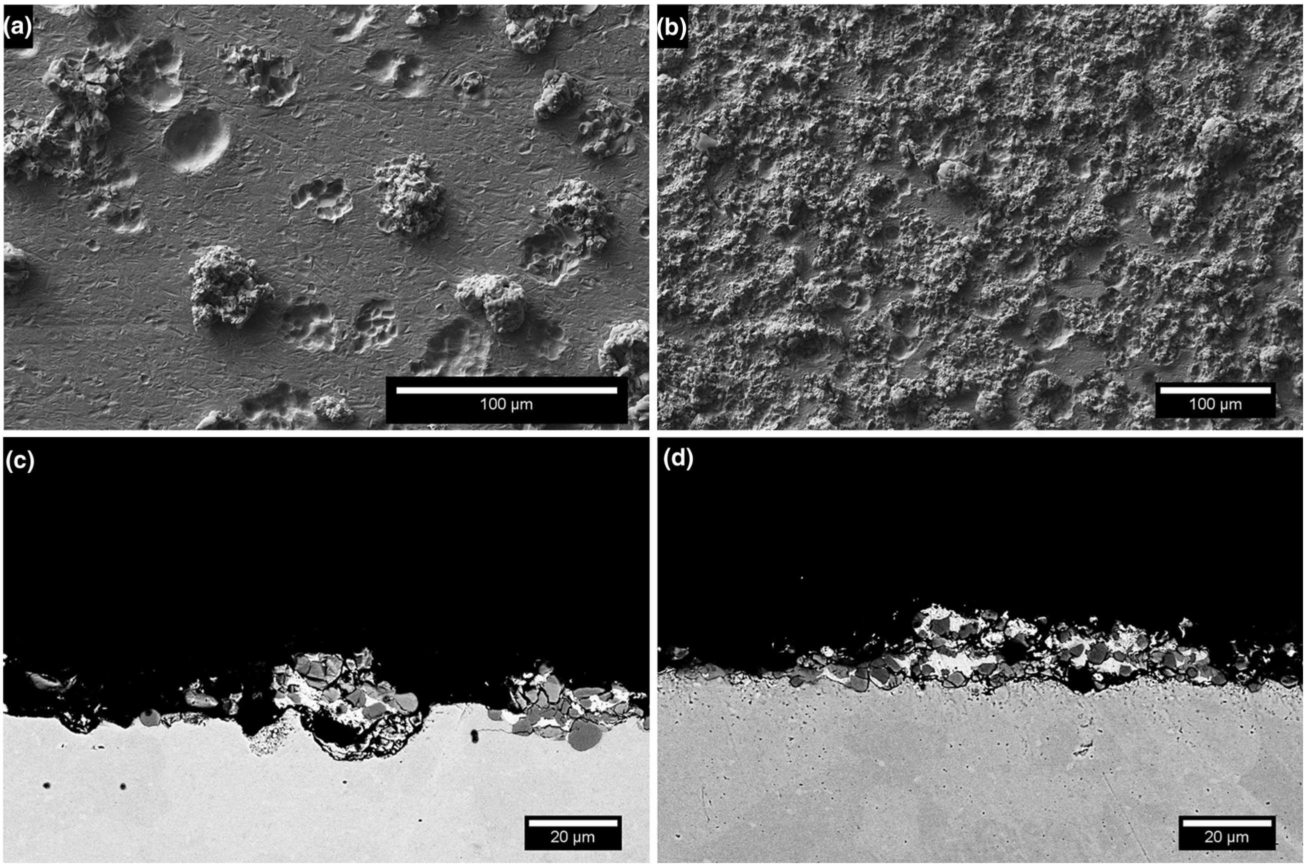

Fig. 23 Interrupted spray test of Amperit 584: (a) and (b) top views; (c) and (d) cross sections

off of some parts of the coatings while spraying are linked. When the coating is being built, cracks propagate until they can no longer sustain the stresses of the deposition, and consequently the stream of gas delaminates a section of the coating. The coatings ceramic/metal ratio was evaluated using EDS, and an increase in the metallic content from 25 wt.% of NiCr in the powder to 41 wt.% in the coating was found.

Interrupted spray test results confirmed the fracture of the particles upon impact. Figure 15 shows some of the first particles that arrived at the substrates and confirms that they have been fractured upon impact. It also reveals that some particles did lose a section of the original particle as it is possible to see NiCr particle components still adhered to the substrate and mixed with ceramic particles on top. Besides the fractured particles, the tests also revealed several craters created by the particles without any particle bonding. The exact bonding mechanism was not revealed by these images, but it is hypothesized that it is a combination of mechanical and metallurgical bonding depending on the particles impacting surface.

This particle fracturing upon impact can also be confirmed upon inspection of the recovered non-adhered particles. It can be observed from Fig. 16 that almost all particles that did no adhere to the substrate fractured upon impact. Even when full particles are found, as presented in Fig. 16(b), these particles are severely cracked in the sections where the ceramic particles were fused. These sections of the particles are weak and brittle locations that promote fracture upon the stresses caused by the impact. This is also supported by the amount of small ceramic particles found in the recovered powder. Upon impact, when a particle cracks and fractures, several of these ceramic particles will be lost, due to the weak bonding between them and will be blown away by the cold spray gas stream, explaining the increment of the NiCr phase in the coatings.

As particles keep adhering to the surface of the previously deposited and cracked particles, the coating keeps building up. This combines with the intrinsic porosity of the feedstock particles and creates porous zones that evolve into cracks. Figure 17 shows a cross section and overview

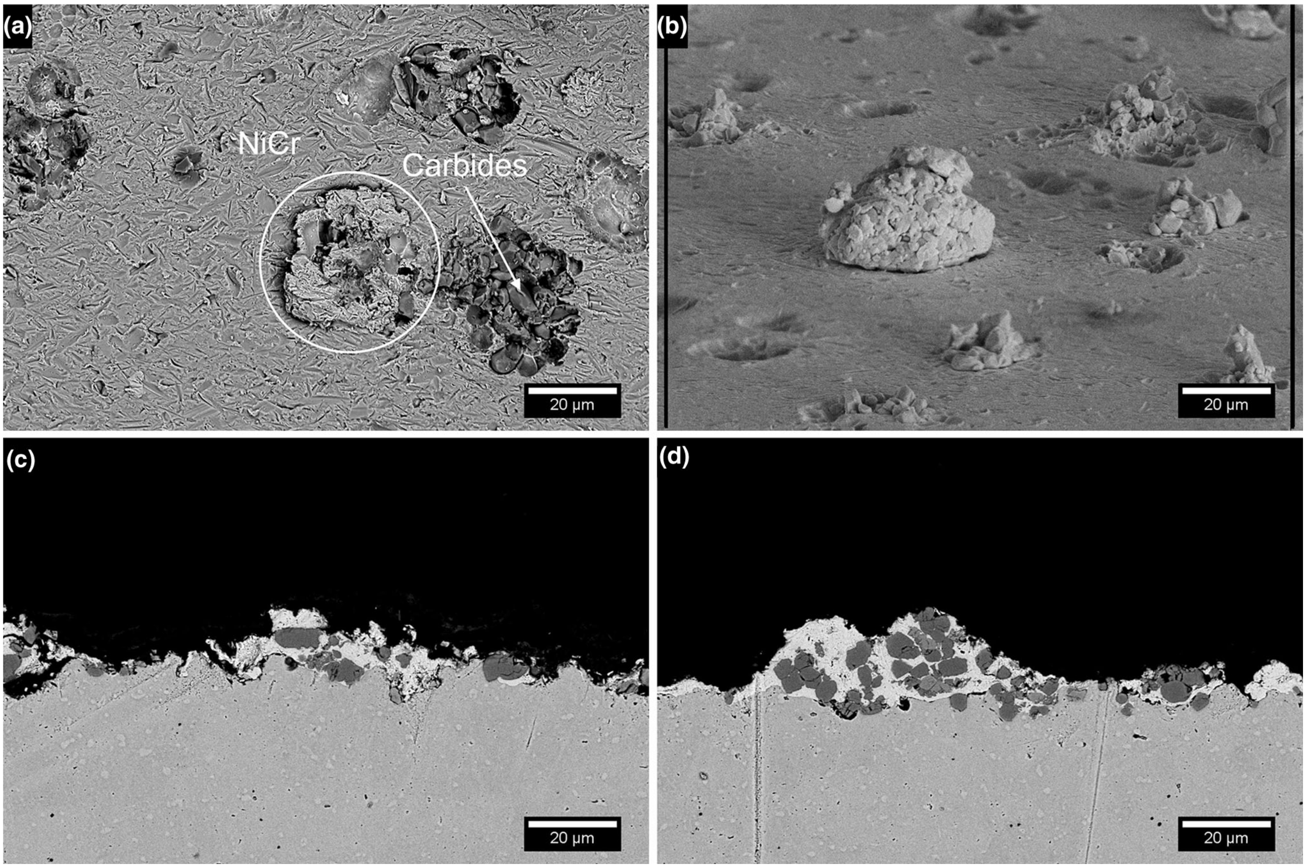

Fig. 24 Interrupted spray test of Amperit 587: (a) and (b) top view; (c) and (d) cross sections

image of the second layer of particles adhering to the substrate. It is easy to see the gap between the particles and the inherent porosity of the particles contributing to the coating porosity. This lack of structural integrity finally results in coating delamination or in the long horizontal cracks present in the coatings cross sections.

Finite element analysis helped to assess the deformation behavior and adhesion mechanism of these porous particles. Some cross-sectioned particles were digitalized and imported to Abaqus/Explicit for impact modeling. Figure 18 shows the digitalized particles used in the finite element analysis. The fused ceramic particles were assumed to behave as a continuous particle. After the simulations, the stress in the fused ceramic contact zones was inspected in order to conclude whether the stresses at these locations were enough to explain the cracking observed experimentally. The substrate temperature was evaluated at 199 °C.

Figure 19 shows the particles deformation at three different stages of the impact. The time steps were defined depending on the kinetic energy of the simulation. Figure 19(a) corresponds to the particles before the impact, when the kinetic energy is the highest. Figure 19(b) represents the midpoint between the highest and the lowest point in kinetic energy, and finally, Fig. 19(c) is the position with the lowest kinetic energy. This last frame is when the particle is at its highest deformation, and before the elastic energy stored in the particle is released. It can be seen that even at this highest deformation point, a single particle does not have enough energy to close the pores originally present in the particles, as all figures show some remnant porosities. This is confirmed experimentally when comparing these images with Fig. 17(a).

Even though these simulations were done without considering damage or fracture of the brittle phase, it is still possible to find insight on the impact mechanism by analyzing stresses and plastic strains experienced by the particles. Figure 20 shows the stress field in two selected particles at the location of the lowest kinetic energy. The display of the stresses has been limited to a minimum of 5 GPa in tension, with this value considerably higher than the flexural strength of Cr_3C_2 particles of these dimensions (Ref 45). Therefore, there is no doubt that the stresses due to impact might fracture these particles. The locations where the stresses are higher (colored sections) are located exclusively inside the ceramic particles and concentrated at fused zoned between ceramic particles. Due to the high stresses, it is expected that these sections should experience fracture of the ceramic particles, leading to the results observed in the interrupted spray tests, where several fracture zones were identified. This can be the reason behind the numerous horizontal cracks seen in Fig. 14 and the peeling of the coatings during deposition.

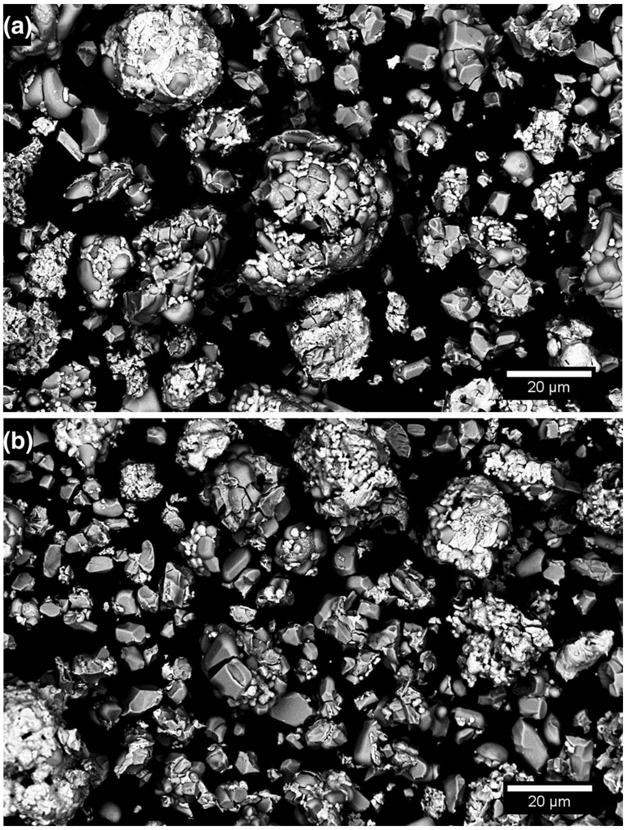

Fig. 25 Overview of non-adhered powders: (a) Amperit 584; (b) Amperit 587

Dense Agglomerated and Sintered Morphology

The third category of powder includes H.C. Starck, Amperit 584 and Amperit 587 powders. Both powders are produced by agglomeration and sintering, but their morphology differs from the CRC-300 powder, as can be seen from Fig. 21. This is true even for Amperit 584 powder (Fig. 21a) that contains 25 wt.% of NiCr, similarly to the previous studied powder CRC-300. This is a result of the powder production techniques used. Different agglomeration techniques, pressures, initial particle sizes and sinterization temperatures can lead to different final morphologies. Figure 21 reveals less apparent porosity than the previously studied agglomerated and sintered powder (CRC-300). Amperit 587, Fig. 21(b) and (d), shows more superficial NiCr than Amperit 584. This is expected due to its higher NiCr content (35 wt.%). Cross sections of both powders, presented in Fig. 21(c) and (d), show that these powders are mostly dense, with some porosity found inside some of the particles.

Even though these powders morphology appears to be similar, their behavior during cold spray deposition differed greatly. The DE of Amperit 584 was evaluated at −0.1, therefore resulting in a slight erosion of the substrate, while the DE of Amperit 587 was evaluated at 4.0%. This

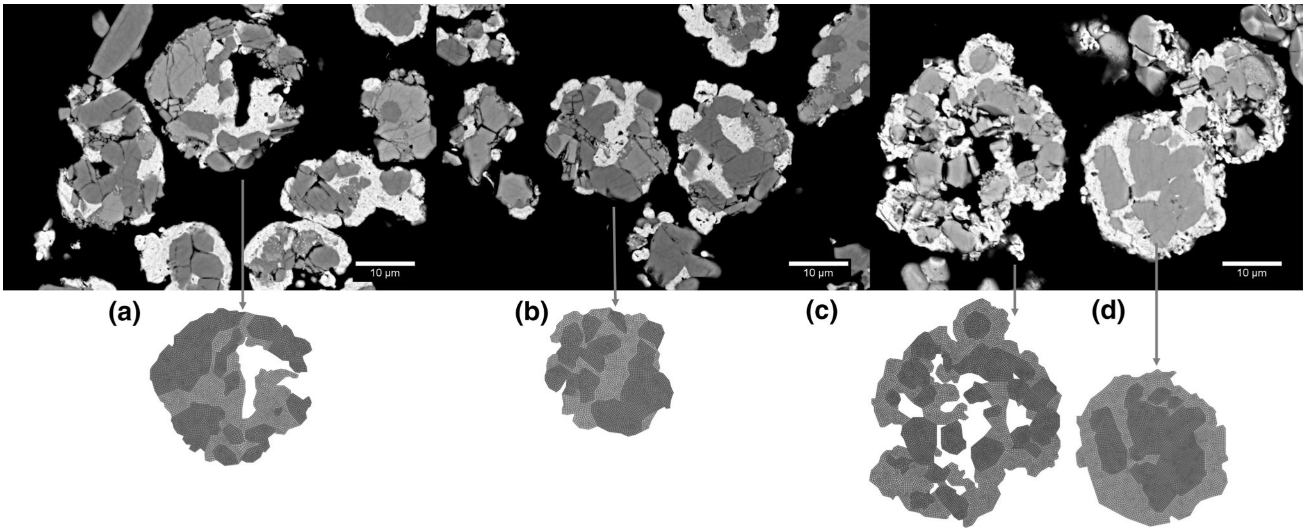

Fig. 26 Digitalization of selected particles: (a) and (b) Amperit 584 powders. (c) and (d) Amperit 587 powders

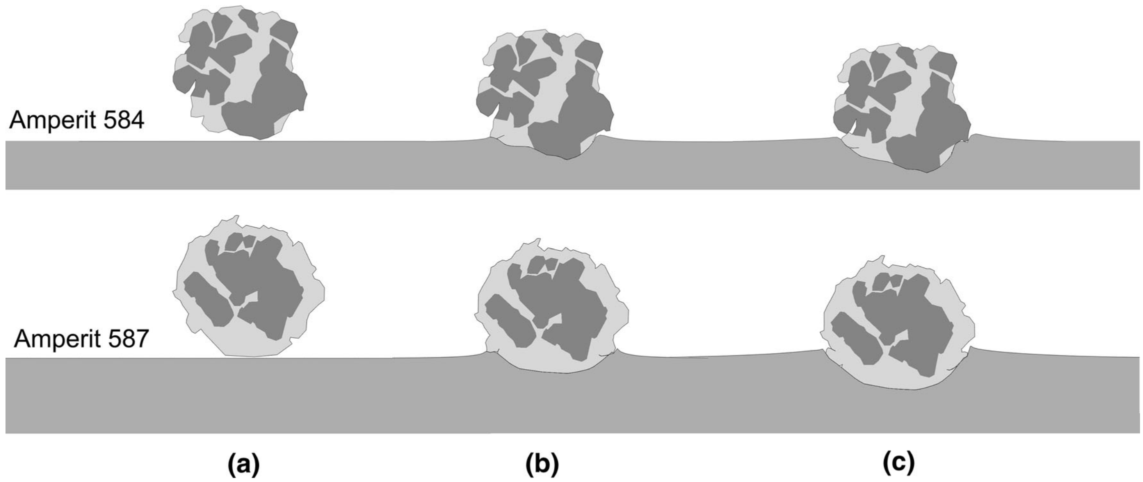

Fig. 27 Evolution of particle deformation at different kinetic energy levels: (a) highest energy level; (b) midpoint; (c) lowest kinetic energy for selected particles, Amperit 584 and Amperit 587

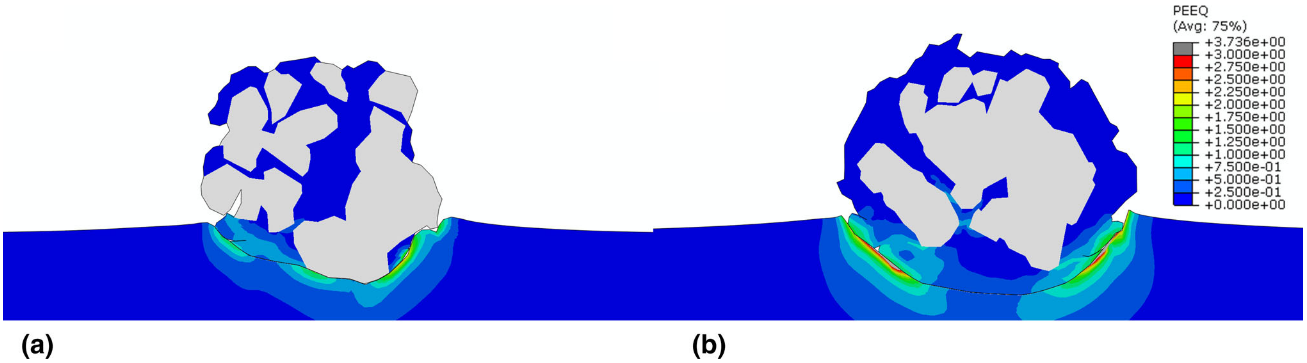

Fig. 28 Plastic deformation field of selected particles: (a) Amperit 584; (b) Amperit 587

difference is attributed to the higher metallic phase content in Amperit 587. The higher amount of NiCr makes the particles more likely to deform and adhere to the substrate. Figure 22 shows a cross section of one of the coatings obtained with the Amperit 587 powder. The coating is dense and does not show any trace of horizontal cracks. The NiCr content of the coatings measured with EDS was evaluated as 60 wt.% NiCr. This value is remarkably high when compared with the original feedstock powder composition (35 wt.%).

Interrupted spray test results gave some indications of the reasons behind this large difference in deposition behavior between the two powders. Even though Amperit 584 resulted in erosion, the tests revealed that the first particles impacting the substrates adhere to it. Figure 23(a) shows several particles, some fragmented by the impact and others intact. As the spray progresses, the particles do not adhere and eventually start eroding the first layer and the substrate, as can be seen in Fig. 23(b). This effect is also shown in cross sections of the tests substrates, where single particles can be found, as illustrated in Fig. 23(c). But when a second particle impacts the adhered particle, both fracture and lose some material leaving just a fragment of the original particles in the substrate, as shown in Fig. 23(d).

Amperit 587 powder shows a similar behavior in the interrupted spray tests. Some of the first particles arriving at the substrate fractured upon impact or left an indentation without adhering. However, the tests also revealed that some particles impact and leave lumps of NiCr at the substrate surface with some ceramic particles adhered to it. These particles are likely the ones with high NiCr content at the surface. An example of the traces left on the substrate can be seen in Fig. 24(a). These particles with high metallic content at the surface can also deposit without fracturing as shown in Fig. 24(b). This behavior is confirmed by the cross sections images in Fig. 24(c) and (d), where the particles are found to have a high NiCr content and just a few ceramic particles. This behavior gets repeated as particles keep depositing. This difference in deposition behavior results in the difference in DE compared to

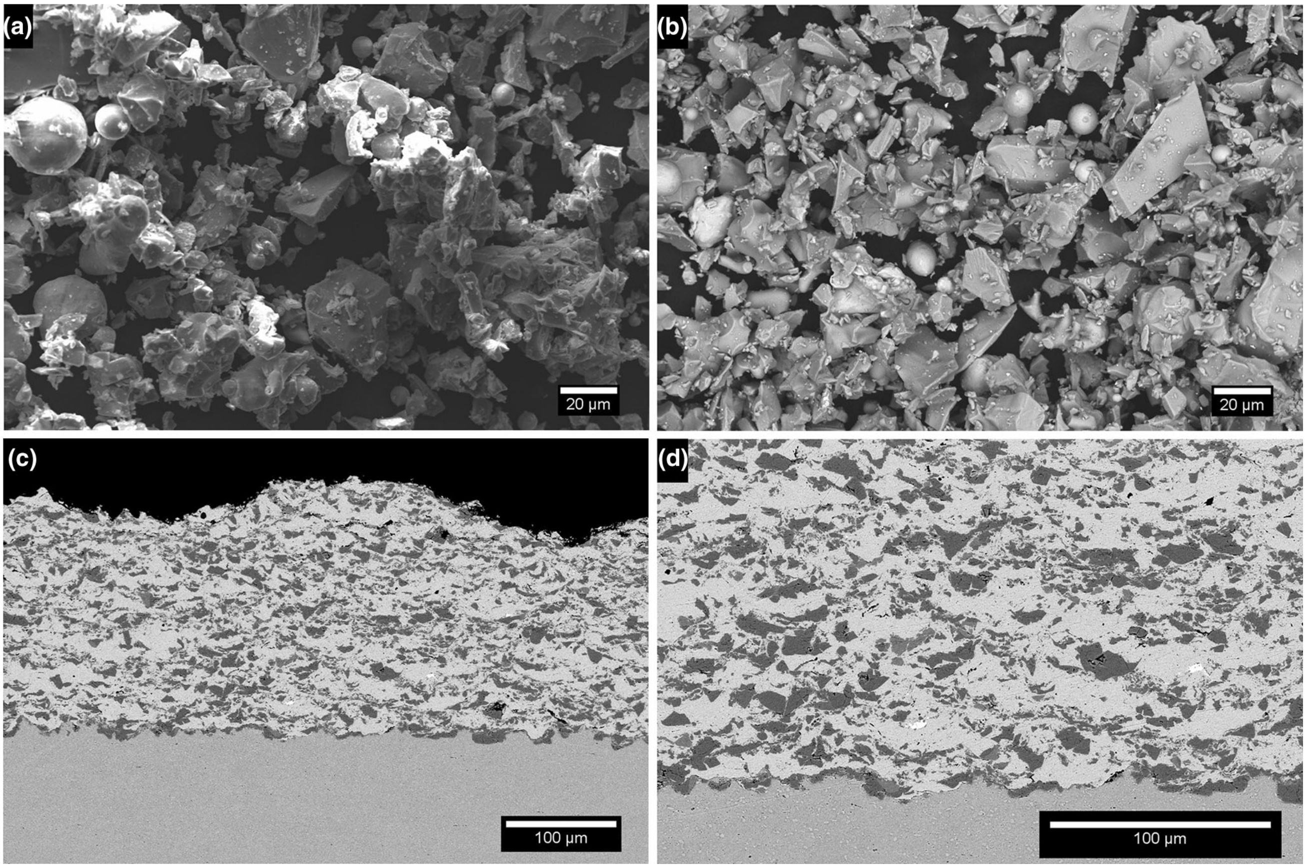

Fig. 29 (a) and (b) Overview of Diamalloy 3004; (c) and (d) cross sections of coatings obtained

Amperit 584. While the Amperit 584 powder deposited the first particles carrying a high ceramic content, it resulted in the erosion of the adhered particles when new incoming particles impacted on the first particles deposited. For the case of Amperit 587 feedstock powder, it deposits preferentially when the metallic phase of the particle impacts the substrate. This allows for the next particles to have a ductile surface to adhered to and allow building the coating. However, this deposition mechanism comes at the cost of low DE and the requirement of limited ceramic content.

The fracturing of the particles observed in the interrupted spray tests results is confirmed by analyzing the particles that did not adhere to the substrate. Figure 25 shows the powder recovered after spray and reveals a high amount of small ceramic particles and also particles fractured in half, possibly as a result of the high stress in this section of the particles. This high amount of ceramic particles is in line with the reduction in coating ceramic content observed when comparing the coatings with the feedstock powders.

For the FEA, some cross-sectioned particles were digitalized and imported to Abaqus/Explicit. Figure 26 shows some of the digitalized particles used in the finite element analysis. The substrate temperature was evaluated at 195 °C.

Figure 27 shows the deformation of some selected particles for each powder at three different kinetic energy levels. Figure 27(a) shows the particles just before the impact with the substrate, at the highest kinetic energy level, Fig. 27(b) midway to the minimum kinetic energy level and Fig. 27(c) at its lowest kinetic energy level. It is easy to see that these particles do not experience much plastic deformation upon impact. This is a consequence of their high density and the strengthening effect of the ceramic particles. Figure 28 displays PEEQ, and it is possible to see that particles with a NiCr outer layer present a higher degree of deformation upon impact at the substrate contact and have a larger area of contact between metal in the particle and the substrate. This allows the superficial metallic layer of the particle to adhere to the substrate. If the ceramic content is not well adhered to the superficial

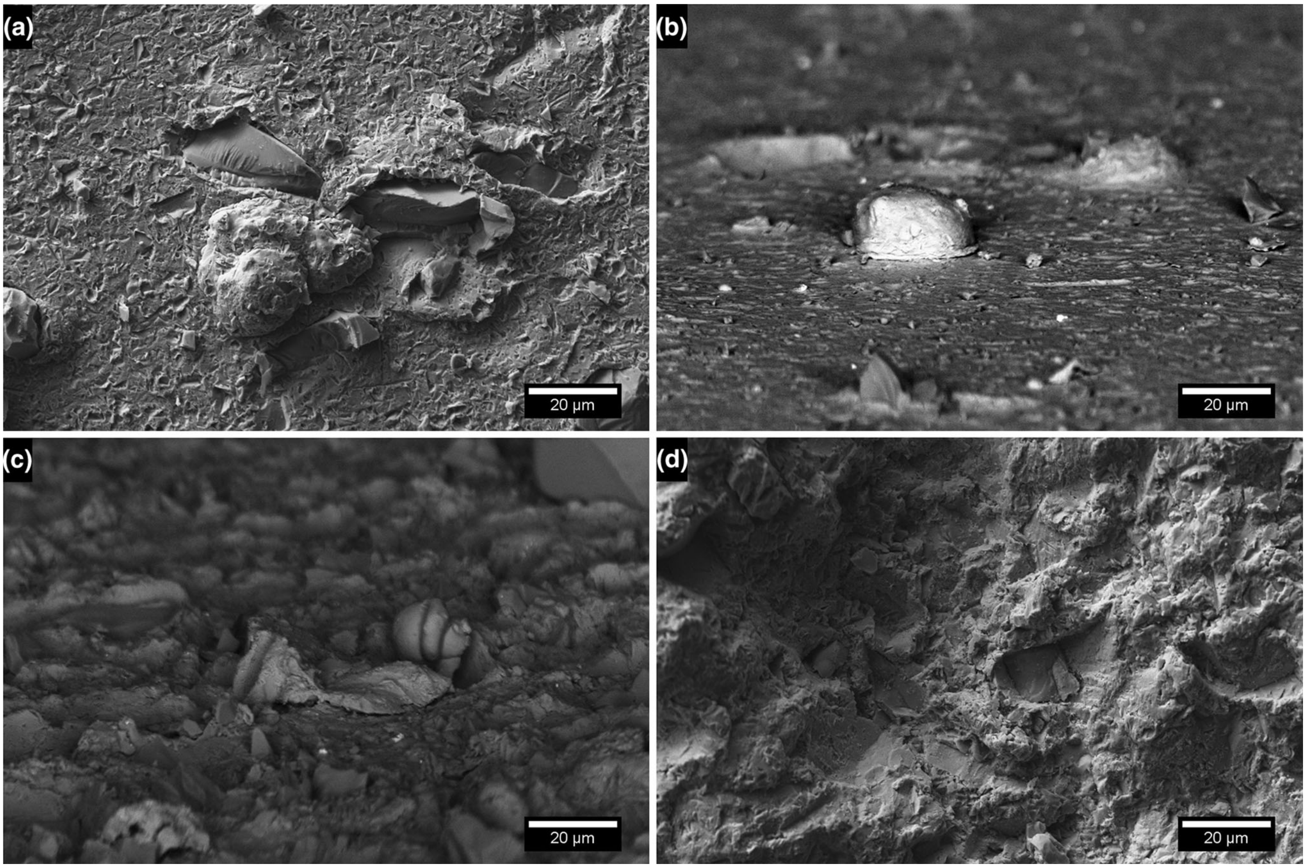

Fig. 30 Interrupted spray test results of Diamalloy 3004: (a) NiCr particle and embedded ceramics; (b) NiCr particles; (c) Peened NiCr particle; (d) top view of coating

metal, a result as the one shown in Fig. 24(a) can be obtained where just remains of NiCr are found in the substrates. In case the ceramic layer adheres well to the metal, a result as illustrated in Fig. 24(b) can be obtained, where the full particle adheres to the substrate. Another feature to observe is the amount of plastic deformation of the substrate that can accommodate or promote particle embedment even if not enough plastic deformation is seen in the particle.

Blended Powders

Diamalloy 3004 was classified as blended powder. This powder is a commercial blending made with atomized 25 wt.% NiCr and 75 wt.% chromium carbide. This morphology is shown in Fig. 29(a) and (b). A large range in ceramic particle size is observed, ranging from 5um to 25 um in size. Deposition of this powder was successful, obtaining dense coatings shown in Fig. 29(c) and (d). The DE of this powder was measured at 4.2%, slightly higher that Amperit 587. The coating metallic content measured by EDS was 69 wt.% NiCr. This value is remarkably higher than the feedstock powder at 25 wt.% of NiCr. This behavior has been previously reported in investigations when the consolidation of blended cermet powders by cold spray has been studied (Ref 26, 29, 46-48). These investigations have covered in general aluminum-based cermets, and it has been seen that the ceramic weight percentage in the coatings reduced approximately to half of the powder content. It is important to note that this study used completely different materials and obtained a low DE compared with the investigation of Al-based cermets, but the reduction in ceramic content seen after deposition is in the same range (from 75 wt.% in the feedstock powder to 31 wt.% of carbide in the coatings).

Interrupted spray tests reveal the deposition behavior of this powder. Figure 30(a) shows that ceramic particles hit and deeply embed the substrates, while Fig. 30(b) shows that NiCr particles deform upon impact, adhering to the substrates. As the deposition continues, the ceramic particles act as peening agent, hitting and deforming the previously deposited material. Figure 30(c) shows a NiCr particle that has been severely deformed by these peening particles. Figure 30(d) shows a top view of the coating obtained with this powder, where just a few ceramic particles can be identified on the surface. This suggests that ceramic particles have lower probabilities of adhering to the substrate that the metallic particles.

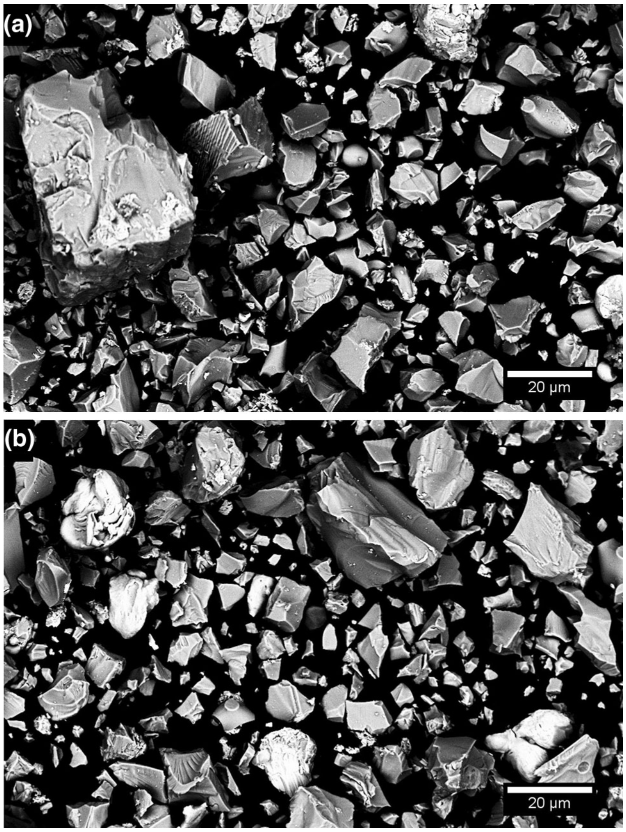

Fig. 31 Overview of Diamalloy 3004 non-adhered powder particles

In addition, when the powders that did not adhere to the substrate (Fig. 31) are analyzed, it is easy to see that most of these particles are ceramic particles. One can also observe that several ceramic particles appear to be fractured. In addition, as expected, the metallic particles recovered appear to be severely deformed.

FEA was also done for this powder, and three cross sections of the carbides and three cross sections of NiCr powders were digitalized and imported to Abaqus/Explicit. Figure 32 shows some selected digitalized particles used in the finite element analysis. The substrate temperature was evaluated at 190 °C.

Figure 33 shows the result of the FEA for some selected particles. The deformation seen in the NiCr particles is characteristic of impacts of spherical metallic particles in cold spray, and it is comparable with result found in the interrupted spray tests (Fig. 30b). Figure 33(c) and (d) shows the FEA results of the ceramic particles. It is important to note the indentation depth of the ceramic particles, leading to particle embedment seen in Fig. 30(a). From the FEA analysis, it is clear the ceramic particles do not embed completely into the substrate, the exposed part of the ceramic particle leaving them vulnerable to breaking by following impacts with incoming particles. When this happens, part of the ceramic particle remains deeply embedded in the substrate and the fractured part flies away as the one seen in Fig. 31. Figure 34 shows an example of the particles that remain embedded in the substrate after fracturing.

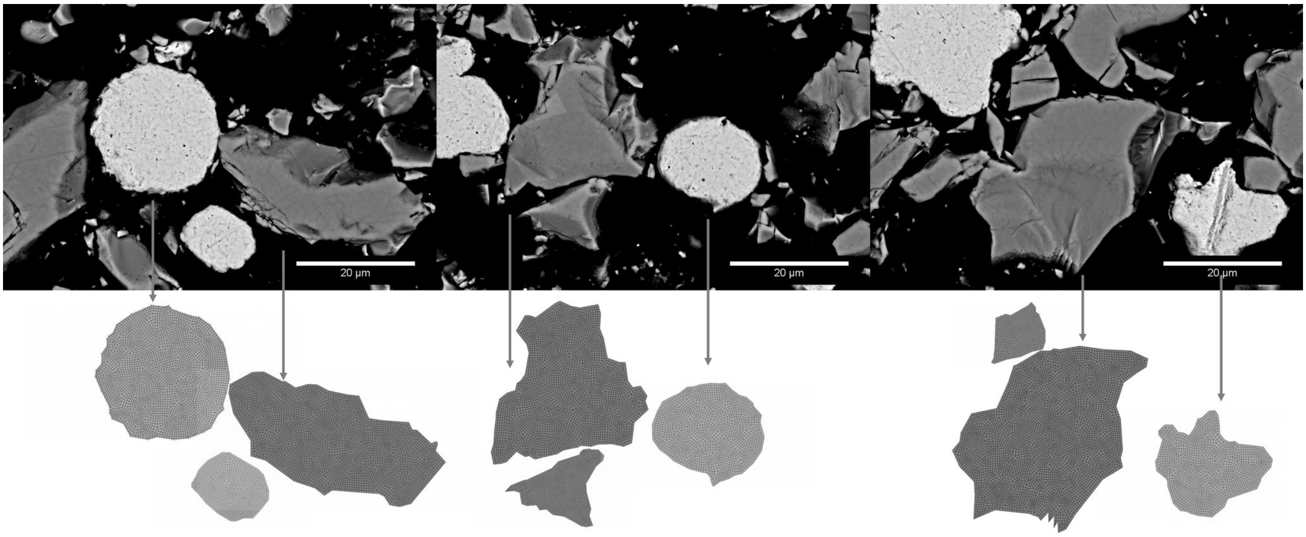

Fig. 32 Ceramic and metallic particle digitalizations used for FEA for Diamalloy 3004

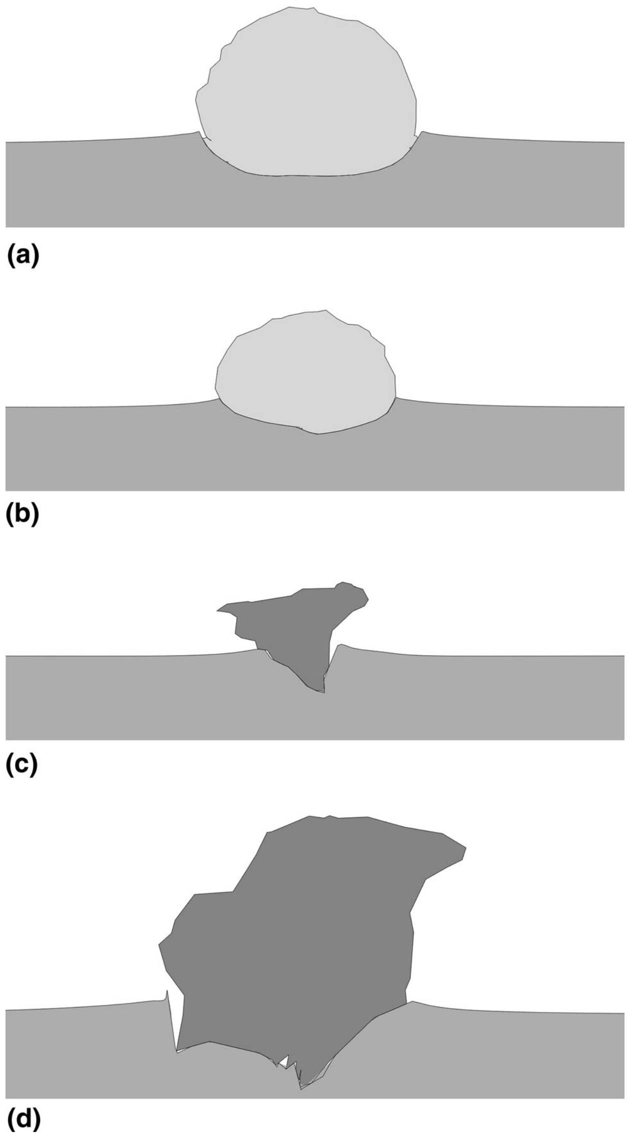

Fig. 33 FEA results for selected Diamalloy 3004 particles: (a) and (b) metallic particles; (c) and (d) ceramic particles

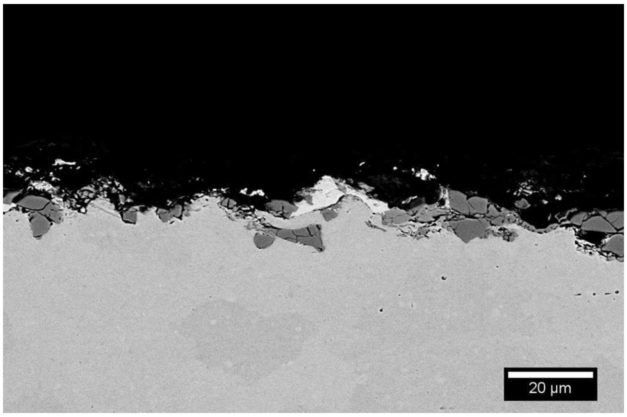

Fig. 34 Fractured chromium carbide particles embedded in the substrate

Summary of Results

Table 6 summarizes the obtained results. It presents the powders used with their respective DE and the ceramic content of the coatings, when coatings were obtained. It is important to note that in all coatings, the ceramic composition was reduced. This is a general outcome seen by other investigations in cermets by cold spray (Ref 26, 29, 46-48). It is important to mention that DEs of these powders are remarkably low. This is a result of the low deposition parameters and the use of nitrogen combined with the hardness of the materials.

Conclusion

From the six CrC-NiCr commercially available powders tested in this investigation, three of them produced coatings, but only two produced dense coatings. The analysis performed allowed identifying that powder morphology has a large impact on the feedstock powder deposition behavior. Both spherical cermets, CRC-410 and CRC-425, led to substrate erosion, the dense particle morphologies leading to low plasticity by redistributing the stresses inside the particles. This lack of ductility is responsible for the low deposition efficiency of these particles. Porous feedstock powder morphologies as the one seen in the CRC-300 powder led to coatings buildup, but several internal cracks were found, leading to coating peeling during deposition. Porous feedstock powder structure with fused ceramic particles at the outside of the particles led to particle fracture upon impact.

Ceramic and metallic contents were also found to be an important factor in the deposition behavior of the particles. Amperit 584 and Amperit 587, both with the same morphology showed different deposition behaviors. Amperit 587 resulted in a dense coating due to its higher metallic content. These particles left metallic traces in the substrate upon impact which helped to build the coatings. Feedstock powders made of metal-ceramic blend also produced dense coatings, even though severe fracturing of the ceramic particles upon impact were observed as well as a high decrease of ceramic content in the coatings. Further studies focusing on this decrease of ceramic content should be done with more accurate methods than EDS. This will allow understanding the structural changes that may happen to the ceramic particles and the potential effect on the coating properties. More studies should be done to characterize and optimize the morphology of cermet powders and tailor them for cold spray in order to widen the spectrum of materials sprayable using this process.

Table 6 Summary of powders used

Commercial name	Morphology	Powder composition, wt.% carbide/metal	DE, %	Coating composition, wt.% carbide/metal
Praxair CRC-410	Spherical	70/30	−0.6 ± 0.2	No deposition
Praxair CRC-425	Spherical	60/40	−0.4 ± 0.1	No deposition
Praxair CRC-300	Porous agglomerated and sintered	75/25	1.7 ± 0.9	59/41
H.C. Starck Amperit 584	Dense agglomerated and sintered	75/25	−0.1 ± 0.1	No deposition
H.C. Starck Amperit 587	Dense agglomerated and sintered	65/35	4.0 ± 0.8	48/52
Oerlikon Diamalloy 3004	Atomized with crushed	75/25	4.2 ± 0.7	31/69

References

1. J.A. Picas, M. Punset, S. Menargues, E. Martín, and M.T. Baile, Microstructural and Tribological Studies of as-Sprayed and Heat-Treated HVOF Cr_3C_2-CoNiCrAlY Coatings with a CoNiCrAlY Bond Coat, *Surf. Coat. Technol.*, 2015, **268**, p 317-324. doi:10.1016/j.surfcoat.2014.10.039
2. G.-C. Ji, C.-J. Li, Y.-Y. Wang, and W.-Y. Li, Microstructural Characterization and Abrasive Wear Performance of HVOF Sprayed Cr_3C_2-NiCr Coating, *Surf. Coat. Technol.*, 2006, **200**(24), p 6749-6757. doi:10.1016/j.surfcoat.2005.10.005
3. D. Poirier, J.-G.G. Legoux, and R.S. Lima, Engineering HVOF-Sprayed Cr_3C_2-NiCr Coatings: The Effect of Particle Morphology and Spraying Parameters on the Microstructure, Properties, and High Temperature Wear Performance, *J. Therm. Spray Technol.*, 2013, **22**(2-3), p 280-289. doi:10.1007/s11666-012-9833-3
4. E. Yun and S. Lee, Correlation of Microstructure with Hardness and Wear Resistance in Cr_3C_2/Stainless Steel Surface Composites Fabricated by High-Energy Electron Beam Irradiation, *Mater. Sci. Eng., A*, 2005, **405**(1-2), p 163-172
5. L. Baiamonte, F. Marra, S. Gazzola, P. Giovanetto, C. Bartuli, T. Valente, and G. Pulci, Thermal Sprayed Coatings for Hot Corrosion Protection of Exhaust Valves in Naval Diesel Engines, *Surf. Coat. Technol.*, 2015, doi:10.1016/j.surfcoat.2015.10.072
6. Y. Ding, T. Hussain, and D.G. McCartney, High-Temperature Oxidation of HVOF Thermally Sprayed NiCr-Cr_3C_2 Coatings: Microstructure and Kinetic, *J. Mater. Sci.*, 2015, **50**(20), p 6808-6821. doi:10.1007/s10853-015-9238-z
7. J.A. Picas, A. Forn, and G. Matthäus, HVOF Coatings as an Alternative to Hard Chrome for Pistons and Valves, *Wear*, 2006, **261**(5-6), p 477-484. doi:10.1016/j.wear.2005.12.005
8. C.T. Kunioshi, O.V. Correa, and L.V. Ramanathan, High Temperature Oxidation and Erosion-Oxidation Behaviour of HVOF Sprayed Ni-20Cr, WC-20Cr-7Ni and Cr_3C_2-Ni-20Cr Coatings, *Surf. Eng.*, 2006, **22**(2), p 121-127. doi:10.1179/174329406X98403
9. B.Q. Wang and K. Luer, The Erosion-Oxidation Behavior of HVOF Cr_3C_2-NiCr Cermet Coating, *Wear*, 1994, **174**(1), p 177-185
10. B.Q. Wang and Z.R. Shui, The Hot Erosion Behavior of HVOF Chromium Carbide-Metal Cermet Coatings Sprayed with Different Powders, *Wear*, 2002, **253**(5), p 550-557
11. S. Matthews, Compositional Development as a Function of Spray Distance in Unshrouded/Shrouded Plasma-Sprayed Cr_3C_2-NiCr Coatings, *J. Therm. Spray Technol.*, 2014, **24**(3), p 515-533. doi:10.1007/s11666-014-0212-0
12. N. Matthews, R. Jones, and G.C. Sih, Application of Supersonic Particle Deposition to Enhance the Structural Integrity of Aircraft Structures, *Sci. China Phys. Mech. Astron.*, 2013, **57**(1), p 12-18. doi:10.1007/s11433-013-5367-z
13. J. Yuan, C. Ma, S. Yang, Z. Yu, and H. Li, Improving the Wear Resistance of HVOF Sprayed WC-Co Coatings by Adding Submicron-Sized WC Particles at the Splats' Interfaces, *Surf. Coat. Technol.*, 2015, doi:10.1016/j.surfcoat.2015.11.017
14. S.A. Alidokht, P. Manimunda, P. Vo, S. Yue, and R.R. Chromik, Cold Spray Deposition of a Ni-WC Composite Coating and Its Dry Sliding Wear Behavior, *Surf. Coat. Technol.*, 2016, **308**, p 424-434
15. J. Yuan, Q. Zhan, J. Huang, S. Ding, and H. Li, Decarburization Mechanisms of WC–Co during Thermal Spraying: Insights from Controlled Carbon Loss and Microstructure Characterization, *Mater. Chem. Phys.*, 2013, **142**(1), p 165-171
16. H. Myalska, G. Moskal, and K. Szymański, Microstructure and Properties of WC-Co Coatings, Modified by Sub-Microcrystalline Carbides, Obtained by Different Methods of High Velocity Spray Processes, *Surf. Coat. Technol.*, 2014, **260**, p 303-309. doi:10.1016/j.surfcoat.2014.07.097
17. R.C.C. Dykhuizen and M.F.F. Smith, Gas Dynamic Principles of Cold Spray, *J. Therm. Spray Technol.*, 1998, **7**(2), p 205-212
18. A.O. Tokarev, Structure of Aluminum Powder Coatings Prepared by Cold Gasdynamic Spraying, *Met. Sci. Heat Treat.*, 1996, **38**(3), p 136-139. doi:10.1007/BF01401446
19. A.P. Alkhimov, A.N. Papyrin, V.F. Kosarev, N.I. Nesterovich, and M.M. Shushpanov, Method and Device for Coating, European Patent 0484533 A4, 1992
20. H. Assadi, F. Gärtner, T. Stoltenhoff, and H. Kreye, Bonding Mechanism in Cold Gas Spraying, *Acta Mater.*, 2003, **51**(15), p 4379-4394. doi:10.1016/S1359-6454(03)00274-X
21. T. Schmidt, H. Assadi, F. Gärtner, H. Richter, T. Stoltenhoff, H. Kreye, and T. Klassen, From Particle Acceleration to Impact and

Bonding in Cold Spraying, *J. Therm. Spray Technol.*, 2009, **18**(5-6), p 794-808

22. M. Grujicic, J.R. Saylor, D.E. Beasley, W.S. DeRosset, and D. Helfritch, Computational Analysis of the Interfacial Bonding between Feed-Powder Particles and the Substrate in the Cold-Gas Dynamic-Spray Process, *Appl. Surf. Sci.*, 2003, **219**(3-4), p 211-227. doi:10.1016/S0169-4332(03)00643-3
23. T. Hussain, D.G. McCartney, P.H. Shipway, and D. Zhang, Bonding Mechanisms in Cold Spraying: The Contributions of Metallurgical and Mechanical Components, *J. Therm. Spray Technol.*, 2009, **18**(3), p 364-379
24. R.C.C. Dykhuizen, M.F.F. Smith, D.L.L. Gilmore, R.A.A. Neiser, X. Jiang, and S. Sampath, Impact of High Velocity Cold Spray Particles, *J. Therm. Spray Technol.*, 1999, **8**(4), p 559-564. doi:10.1361/105996399770350250
25. T. Samson, D. MacDonald, R. Fernández, and B. Jodoin, Effect of Pulsed Waterjet Surface Preparation on the Adhesion Strength of Cold Gas Dynamic Sprayed Aluminum Coatings, *J. Therm. Spray Technol.*, 2015, **24**(6), p 984-993. doi:10.1007/s11666-015-0261-z
26. E. Irissou, J.-G. Legoux, B. Arsenault, and C. Moreau, Investigation of Al-Al2O3 Cold Spray Coating Formation and Properties, *J. Therm. Spray Technol.*, 2007, **16**(5-6), p 661-668. doi:10.1007/s11666-007-9086-8
27. A. Sova, A. Papyrin, and I. Smurov, Influence of Ceramic Powder Size on Process of Cermet Coating Formation by Cold Spray, *J. Therm. Spray Technol.*, 2009, **18**(4), p 633-641. doi:10.1007/s11666-009-9359-5
28. Q. Wang, K. Spencer, N. Birbilis, and M.-X. Zhang, The Influence of Ceramic Particles on Bond Strength of Cold Spray Composite Coatings on AZ91 Alloy Substrate, *Surf. Coat. Technol.*, 2010, **205**(1), p 50-56. doi:10.1016/j.surfcoat.2010.06.008
29. A. Shkodkin, A. Kashirin, O. Klyuev, and T. Buzdygar, Metal Particle Deposition Stimulation by Surface Abrasive Treatment in Gas Dynamic Spraying, *J. Therm. Spray Technol.*, 2006, **15**(3), p 382-386
30. I. Finnie and D.H. McFadden, On the Velocity Dependence of the Erosion of Ductile Metals by Solid Particles at Low Angles of Incidence, *Wear*, 1978, **48**(1), p 181-190. doi:10.1016/0043-1648(78)90147-3
31. A.S.M. Ang, C.C. Berndt, and P. Cheang, Deposition Effects of WC Particle Size on Cold Sprayed WC-Co Coatings, *Surf. Coat. Technol.*, 2011, **205**(10), p 3260-3267. doi:10.1016/j.surfcoat.2010.11.045
32. M. Jafari, M.H. Enayati, M. Salehi, S.M. Nahvi, S.N. Hosseini, and C.G. Park, Influence of Nickel-Coated Nanostructured WC-Co Powders on Microstructural and Tribological Properties of HVOF Coatings, *J. Therm. Spray Technol.*, 2014, **23**(8), p 1456-1469. doi:10.1007/s11666-014-0171-5
33. R. Lima, J. Karthikeyan, C. Kay, J. Lindemann, and C. Berndt, Microstructural Characteristics of Cold-Sprayed Nanostructured WC-Co Coatings, *Thin Solid Films*, 2002, **416**(1-2), p 129-135. doi:10.1016/S0040-6090(02)00631-4
34. D.E. Wolfe, T.J. Eden, J.K. Potter, and A.P. Jaroh, Investigation and Characterization of Cr_3C_2-Based Wear-Resistant Coatings Applied by the Cold Spray Process, *J. Therm. Spray Technol.*, 2006, **15**(3), p 400-412. doi:10.1361/105996306X124400
35. H. Singh, T.S. Sidhu, J. Karthikeyan, and S.B.S. Kalsi, Development and Characterization of Cr3C2-NiCr Coated Superalloy by Novel Cold Spray Process, *Mater. Manuf. Process.*, 2015, **2014**, p 1-7. doi:10.1080/10426914.2014.973599
36. D. MacDonald, R. Fernández, F. Delloro, and B. Jodoin, Cold Spraying of Armstrong Process Titanium Powder for Additive Manufacturing, *J. Therm. Spray Technol.*, 2016, doi:10.1007/s11666-016-0489-2
37. G.R. Johnson and W.H. Cook, A Constitutive Model and Data for Metals Subjected to Large Strains, High Strain Rates and High Temperatures, in *Proceedings of the 7th International Symposium on Ballistics*, The Hague, The Netherlands (1983), pp. 541–547.
38. H.-J. Choi, M. Lee, and J.Y. Lee, Application of a Cold Spray Technique to the Fabrication of a Copper Canister for the Geological Disposal of CANDU Spent Fuels, *Nucl. Eng. Des.*, 2010, **240**(10), p 2714-2720. doi:10.1016/j.nucengdes.2010.06.038
39. S. Yin, Y. Xie, X. Suo, H. Liao, and X. Wang, Interfacial Bonding Features of Ni Coating on Al Substrate with Different Surface Pretreatments in Cold Spray, *Mater. Lett.*, 2015, **138**, p 143-147. doi:10.1016/j.matlet.2014.10.016
40. Y. Cormier, P. Dupuis, B. Jodoin, and A. Ghaei, Finite Element Analysis and Failure Mode Characterization of Pyramidal Fin Arrays Produced by Masked Cold Gas Dynamic Spray, *J. Therm. Spray Technol.*, 2015, **24**(8), p 1549-1565. doi:10.1007/s11666-015-0317-0
41. X. Wang, F. Feng, M.A. Klecka, M.D. Mordasky, J.K. Garofano, T. El-Wardany, A. Nardi, and V.K. Champagne, Characterization and Modeling of the Bonding Process in Cold Spray Additive Manufacturing, *Addit. Manuf.*, 2015, **8**, p 149-162. doi:10.1016/j.addma.2015.03.006
42. P.C. King, G. Bae, S.H. Zahiri, M. Jahedi, and C. Lee, An Experimental and Finite Element Study of Cold Spray Copper Impact onto Two Aluminum Substrates, *J. Therm. Spray Technol.*, 2010, **19**(3), p 620-634. doi:10.1007/s11666-009-9454-7
43. R. Ghelichi, S. Bagherifard, D. Macdonald, I. Fernandez-Pariente, B. Jodoin, and M. Guagliano, Experimental and Numerical Study of Residual Stress Evolution in Cold Spray Coating, *Appl. Surf. Sci.*, 2014, **288**, p 26-33. doi:10.1016/j.apsusc.2013.09.074
44. A. Papyrin, V. Kosarev, S. Klinkov, A. Alkhimov, and V.M. Fomin, *Cold Spray Technology* (Elsevier, Amsterdam, 2006). https://books.google.cl/books?id=XjZMWNVvgLAC
45. C.-T. Fu and J.-M. Wu, Microstructure and Mechanical Properties of Cr_3C_2 Particulate Reinforced AI203 Matrix Composites, *J. Mater. Sci.*, 1994, **29**, p 2671-2677
46. J.M. Shockley, S. Descartes, P. Vo, E. Irissou, and R.R. Chromik, The Influence of Al2O3 Particle Morphology on the Coating Formation and Dry Sliding Wear Behavior of Cold Sprayed Al-Al2O3 Composites, *Surf. Coat. Technol.*, 2015, **270**, p 324-333. doi:10.1016/j.surfcoat.2015.01.057
47. A. Sova, V.F. Kosarev, A. Papyrin, and I. Smurov, Effect of Ceramic Particle Velocity on Cold Spray Deposition of Metal-Ceramic Coatings, *J. Therm. Spray Technol.*, 2010, **20**(1-2), p 285-291. doi:10.1007/s11666-010-9571-3
48. R.G. Maev and E. Leshchinsky, Low Pressure Gas Dynamic Spray: Shear Localization During Particle Shock Consolidation, *Thermal Spray 2006: Science, Innovation and Application on CD-ROM*, B. Marple, M. Hyland, Y.-C. Lau, R. Lima, and J. Voyer, Ed., May 15-18, 2006 (Seattle, WA), ASM International, 2006, 1480 p
49. H.A. Abdel-Aal, On the Influence of Thermal Properties on Wear Resistance of Rubbing Metals at Elevated Temperatures, *J. Tribol. Am. Soc. Mech. Eng.*, 2000, **122**(3), p 657. doi:10.1115/1.555417
50. D.R. Lide, *CRC Handbook of Chemistry and Physics*, 84th edn (Taylor & Francis, London, 2003). https://books.google.cl/books?id=kTnxSi2B2FcC
51. M. Bauccio, *ASM Engineered Materials Reference Book* (ASM International, Seattle, 1994). https://books.google.cl/books?id=f3xUAAAAMAAJ.
52. M.W.J. Chase, *NIST-JANAF Thermochemical Tables* (American Institute of Physics, College Park, 1998). https://books.google.cl/books?id=n5p9RAAACAAJ.

53. E. Uhlmann, M.G. von der Schulenburg, and R. Zettier, Finite Element Modeling and Cutting Simulation of Inconel 718, *CIRP Ann. Manuf. Technol.*, 2007, **56**(1), p 61-64
54. D. Steinberg, *Equation of State and Strength Properties of Selected Materials* (Lawrence Livermore National Laboratory, Livermore, 1996). https://books.google.cl/books?id=UyEXHAAACAAJ.